



**Politecnico
di Torino**

Politecnico di Torino

Master's degree course Aerospace Engineering

Academic year 2021/2022

Graduation Session April 2022

**Neighbour statistical analysis for the dispersion in
clouds by the means of mini green radiosonde**

Thesis associated with the EU project H2020

MSCA ITN ETN COMPLETE

Supervisor:

Prof.ssa Daniela Tordella

Candidate:

Chiara Geron

Abstract

The clouds contribute to environmental system is enormous; clouds can produce solid and liquid water through a series of physical phenomena that take place at different spacial scales. The presence or absence of clouds is essential for many weather aspects. The understanding of both the chemistry and physics of clouds can lead to a wider knowledge of the chemistry and physics of real-world phenomena. Clouds' processes take place at different spacial scales, the phenomena that occur at the micro scale are non-generally visible to human eye. Humans see the macroscopic scales, the net consequence of the light, coming from the sun, scattered by the presence of water drops and small ice crystals inside clouds. In particular warm clouds can contain thousands of different sizes of droplets, but every raindrop that fall to the ground is the result of million clouds' droplets that has gathered together. The uncertainties related to the processes that involve the formation, the structure and the life of clouds are still nowadays subject of studies and research. The COMPLETE project, a Horizon2020 program, has the aim to widen current knowledge about those processes and phenomena inside clouds that involve nonlinear and turbulent flows. The experimental part of this project aims to follow the motion of particles inside clouds in a Lagrangian way thanks to the use of mini probes that can measure proprieties as temperature, pressure, humidity, velocity and trajectory and then send these data to a ground receiver. Those probes are able to fluctuate thanks to biodegradable balloons that float along whit the main stream. In this thesis will be illustrated the current state of knowledge about these arguments and then will be presented the structure and architecture of the probe developed so far with some data measured during tests.

Index

Chapter 1

Introduction.....	5
-------------------	---

Chapter 2

Clouds as a source of uncertainty.....	7
2.1 Classification of clouds.....	8
2.1.1 Clouds forms.....	8
2.2 Warm clouds origin.....	11
2.2.1 CNN activation.....	12
2.2.2 Growth for diffusion and condensation of water vapour.....	13
2.2.3 Growth for collision and coalescence.....	14
2.3 Clouds structure.....	14
2.4 Turbulence.....	16
2.4.1 Turbulence and the developments of droplets.....	17
2.4.2 Droplets motion.....	18
2.5 Entrainment.....	20
2.5.1 Entrainment's mechanism.....	20
2.5.2 Entrainment's consequences.....	21
2.6 Richardson model of atmospheric diffusion and distance-neighbour graph.....	23
2.6.1 DNS model.....	24

Chapter 3

The radiosonde.....	33
3.1 Ultralight radiosonde system Architecture and Design Methodology.....	34

3.2 PCB structure.....	35
3.3 Balloon's material.....	39

Chapter 4

Balloon.....	43
4.1 Preventive estimation.....	43
4.2 Dimentions.....	45
4.3 Assembly.....	46
4.3.1 Instrumentation.....	46
4.3.2 Procedure.....	47

Chapter 5

Data obtained from experiments.....	51
5.1 INRiM experiment.....	51
5.2 OAVdA experiment.....	66

Chapter 6

Conclusions and developments.....	76
References.....	80

Chapter 1

Introduction

Modeling clouds has been a challenge for decades as they depend on a variety of chemical and physical processes ranging from the nanometer scale, where nucleation, coalescence and rain formation take place, to airflow dynamics which can range up to kilometers [1].

However, the non-linear and turbulent dynamic of clouds complicates the system and in-situ measurements are needed to better understand the small-scales fluctuations in velocity, temperature, humidity, pressure, etc [2]

The innovative, ultralight radiosondes, developed as part of the Horizon2020 Innovative Training Network Cloud-MicroPhysics-Turbulence –Telemetry (MSCA-ITN-COMLETE) project, aim at addressing the gap between knowledge and lack of experiments [3].

They are designed to passively track fluctuations of temperature, humidity, pressure and velocity for several hours on isopycnic surfaces in cloud and clear air environments at altitudes between 1-3 km. To reach this goal the radiosonde must transmit data to a receiver station, inside the probe are present different types of sensors that produce data and a battery. The probe is linked to a balloon, with specific properties, that let the probe follow the air stream in a Lagrangian way. Furthermore, to minimize their environmental impact, the design of the balloons is made with biodegradable materials tailored to have specific properties, such as hydrophobicity and flexibility. The development and specialization of these materials is presented along with the first tests of the radiosonde in climate chambers where fluctuations in temperature, pressure and wind velocity can be manually applied [1].

These hydrophobic, lightweight balloons will fill in the existing gap between transoceanic NOAA smart balloons [4] and high-resolution research aircrafts, as the CIRPAS Twin Otter that is an aircraft supports atmospheric and oceanographic research [5] with the aim of providing an insight into the unsteady life cycle of warm clouds over land, ocean and alpine environments. These explorative observations are essential for the contribution and development of the current understanding of microphysical processes in and around clouds to ultimately improve weather prediction and climate models [1].

In the following chapter, which is mainly bibliographic, some information about the current knowledge regarding the formation, the structure and nature of clouds are presented. In the third chapter the structure of the probe's system is explained. The fourth chapter analyses the structure of the balloon and how it is manually produced. Chapter five shows the data measured during two different experiments hold in different external conditions and the how they can be analyzed to produce insights about the air flow. Chapter six is dedicated to conclusions and further improvements that can be done to overcome problems and issues.

Chapter 2

Clouds as source of uncertainty

Clouds, as a complex feature of the Earth environment, are fundamental to humankind in many ways: they control the hydrological cycle, they regulate local and global radiative balances in the atmosphere, they behave as energy traps and they play an active part in determining changes in atmospheric dynamics.

Yet clouds constitute the most poorly quantified, least understood, and most puzzling aspect of atmospheric science, and thus the largest source of uncertainty in the prediction of climate change [6].

Clouds have long been identified as a principal cause of uncertainty in future atmospheric and climate previsions. In order to anticipate and evaluate climate change and in order to forecast regional weather, we must understand the behavior of clouds in the atmosphere, where many interactions with natural and anthropogenic pollutants take place.

Although clouds affect phenomena that occur on large spatial dimensions, the proprieties of clouds that cause their large-scale effects are by nature coupled to their finest dynamics and microphysics [7].

Clouds have been the subject of observation for centuries, but systematic investigations began only a few decades ago. For all practical purposes, the study of clouds can be traced back to Luke Howard, the English pharmacist who began, around 1803, the system of naming cloud types that we still use today. One aspect not yet understood is the fact that inside clouds the kinetic energy is larger than in the clear air outside. Energy can be developed by inner physical-chemical processes as latent heat release by water drops nucleation and condensation or by turbulent energy amplification induced by unstable density stratification. Energy captured from acoustic-gravity waves propagating into clouds from below or above cloud layers, or from cosmic rays during their interaction with water drops, or from electromagnetic radiations from the Earth or from outside the atmosphere should be also considered [61]. Direct observations from balloons and aircraft helped greatly to develop a base of empirical knowledge upon which the research community could later build testable hypotheses. With ongoing improvements in instrumentation and measurement techniques, the invention of cloud chambers, and an ability to test hypotheses quantitatively, the research community of atmospheric scientists has gradually developed a broad and quantitative understanding of clouds. The atmosphere is a mixture of a huge

number of chemical compounds, some gaseous, some particulate in nature. Indeed, water is just one of those myriad components, but the only one of note that changes phase under ordinary conditions. The atmosphere is far more than “dry air” and water vapor, so any modern treatment of clouds must deal with this mixture head-on. Indeed, cloud droplets form on the more soluble subset of the particulate matter, and they subsequently absorb some of the trace gases. The microphysical properties, even the macrophysical forms, of clouds are significantly affected by the chemicals in the air. In turn, many of those chemicals are altered and removed from the atmosphere by clouds and the precipitation they produce. The physics and chemistry of the atmosphere go hand in hand when developing a complete picture of clouds and how they behave in the atmosphere [8].

2.1 Classification of clouds

The naming of cloud types began in the early 1800s. Jean Babtiste Lamarck, a French naturalist, proposed a naming scheme that did not catch on probably because of the French terms he used. Lamarck is, however, credited with proposing that clouds should be identified with the level (high, middle, or low) at which they appear in the atmosphere. Then, within a year or so, Luke Howard, an English chemist/pharmacist, suggested that clouds could be grouped into four main categories, named with a simple Latin terminology: Cirrus (Latin for hair curl), Cumulus (heap), Stratus (layer), and Nimbus (rain).

Clouds are classified into ten genera each of which can have several species and varieties. Clouds in layers are shown on the left side of figure 2.1, whereas clouds that develop vertically, possibly spanning several levels, are shown on the right [8].

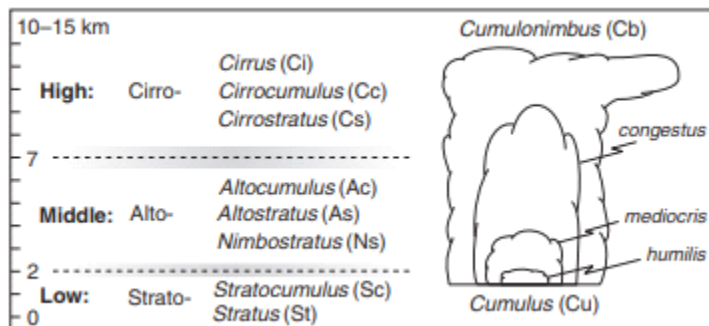


Figure 2.1: Schematic summary of the major cloud types [8]

2.1.1 Clouds forms

Different types of clouds are proposed in bibliography, because of their uncertainty and instability a simplified classification is presented below.

- *Stratiform clouds* are the most stable type. This kind of cloud presents generally flat, sheet-like structures and it rarely produce precipitation. It is common to found them at every level of the troposphere and they usually do not produce precipitations.



Figure 2.2: stratiform clouds [9]

- *Cirriiform clouds* are in filament forms (Figure 2.3) and they are mostly stable. This kind of cloud is present only at high tropospheric altitudes and usually does not produce precipitations.



Figure 2.3: cirriiform clouds [10]

- *Stratocumuliform clouds* embody both stratiform and cumuliform characteristics. These clouds are generally stable, and precipitations depend on altitude at which the cloud is located.



Figure 2.4: stratocumuliform clouds [11]

- *Cumuliform clouds* have greater instability as their dimension grow. This type of cloud has heaps or tufts shapes and might be low-level or multi-level (in this case precipitations remains abundant).



Figure 2.4: cumuliform clouds [12]

- *Cumulonimbform clouds* develop vertically, and they are characterized by high turbulence and instability and can produce moderate to heavy rains.



Figure 2.5: cumulonimbform clouds [13]

2.2 Warm clouds origin

Warm clouds are typically observed at a height of 1000-2000 meters and live for periods that could last some hours up to a couple of days. Those clouds continuously vary their shape and have dimensions in the range of hundreds of meters; the timescale of these variations is of the order of 100 seconds.

These clouds form when there is an adequate supply of water vapor, aerosol particles, and a mechanism for cooling the air. Water in condensed form is the principal component for any cloud, the aerosol particles provide the sites for condensation where water vapor can adhere. Finally cooling lets condensation start, indeed the system temperature fall below the dew point and the vapor exceed the equilibrium value. The atmospheric pressure gradients cause the macroscopic air motion, the water vapor and aerosol particles are lifted, air cools and creates excess water vapor. A parcel of air generally lifts because of convection caused by large scale motion or by the presence of mountains or other orographic structures. The microphysical processes, driven initially by aerosol abundance, determine how the excess vapor is used within the cloud.

Warm clouds generally rise in the lower troposphere; the formation of warm cloud depends on the rise of moist air. At the beginning all warm clouds follow a similar pattern based on the condensation of water vapor around aerosol particles and on the growth of liquid droplets. Next phases during the development of the mature cloud include collisions, coalescence and disruption. When air rises, expand and cools to the dew point clouds are formed; this mechanism is named *adiabatic cooling* and is the most habitual way in which clouds originate. Other ways of cooling are radiational, conductive and evaporative.

Air is at the beginning subsaturated and has inside dry aerosol particles of different sizes, much of the population has a $0.02\mu\text{m}$. As air lifts relative humidity increases, liquid droplets grow around aerosol particles and increase their dimensions by condensation. Warm clouds are at the beginning a stable structure formed by little liquid droplets that move following air and don't directly interact with each other. In order to break the colloidal stability condensation isn't enough, collection must happen. In figure 2.6 is shown the difference between the mechanism of condensation and collection, the *growth gap* represents the uncertain processes by which droplets increase to the size needed for the collision-coalescence growth (collection). Collection is the mechanism by which some big droplets collide and

coalesce in larger droplets, this process requires droplets radii larger than $20\mu\text{m}$. When the colloidal stability is broken a warm-rain process takes over and a large amount of water is removed from the atmosphere. [8]

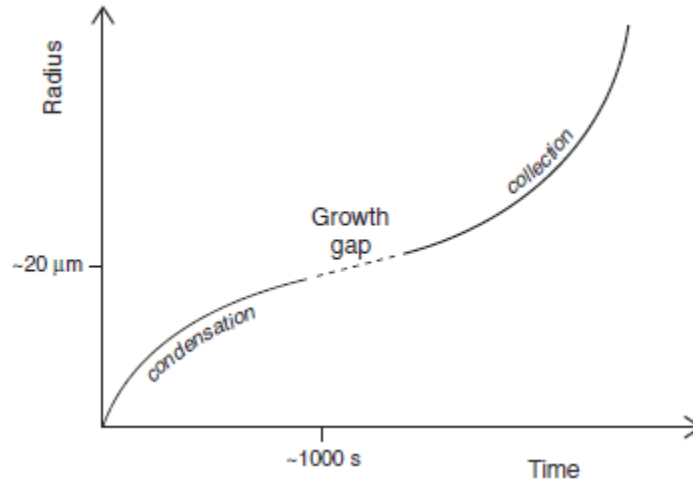


Figure 2.6: Relative growth of drops by condensation and collection; droplets with a radius smaller than $20\mu\text{m}$ grow by condensation, the *growth gap* represents the uncertain processes by which droplets increase to the size needed for the collection process [8]

In order to summarize, in warm clouds the activation and formation of droplets that have a raindrop size take place in three moments:

- Cloud Condensation Nuclei CCN activation
- Condensation and diffusion of water vapor
- Collision and coalescence, collection mechanism

2.2.1 CNN activation

CCNs are aerosol particles with diameters of some micron, originated by micro-particles as dust or chloride that are hygroscopic, so that water vapor gathers around and condensates. Has been observed that the number of CCN increases with the supersaturation and CNN concentration may vary a lot with increasing altitude [14].

During the formation of the cloud, as already mentioned, supersaturation rises and larger and most effective CNN are the first to be activated, then smaller ones. When supersaturation stops to grow the CNN activation phase ends and growth due to condensation and diffusion begins, at this point the average radius of a micro-droplet is 1 μm [15] [16].

2.2.2 Growth for diffusion and condensation of water vapor

Drops growth rate due to condensation follow the equation

$$\frac{dr}{dt} \propto \frac{s}{r}$$

The rate of growth is inversely proportional to the dimension of the radius: small drops increase faster than droplets with larger radii. However, drops don't have the same supersaturation level because in the real atmospheric system they don't evolve as independent adiabatically cells. In figure 2.7 is shown that the resulting spectrum of drops after condensation mechanism isn't as narrow as numerical formula suggest. The fact that the spectrum is wider helps the mechanism of coalesce [17]. Diffusion and condensation involve droplets with radii of 15-20 μm [16].

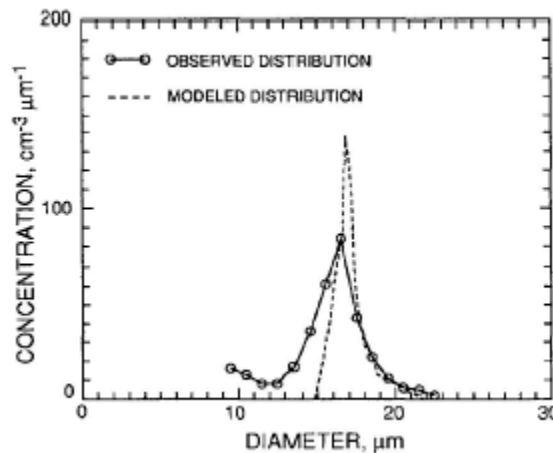


Figure 2.7: spectrum of drops' sizes after condensation process, in particular the mathematical model gives a distribution narrower than the observed one. A wider spectrum increases the rate of the coalescence process [17]

2.2.3 Growth for collisions and coalescence

In this phase larger droplets increase in dimensions capturing smaller droplets due to gravitational collisions, this process become effective when the radius of drops is about 40 μm . Small droplets tend to follow streamlines of the air flowing around large ones, while larger droplets are hindered to do it because of their inertia, so they coalesce. This process means that the frequency of droplets collisions depends on the droplet spectrum width. As mentioned in the previous paragraph a wider spectrum favors coalescence [18].

Altitude is an aspect that plays an important role in the coalescence phase, it can increase the terminal velocity of the droplet from 5% to 20% and enhance the collision efficiency: lower air pressure and density values would make the motion of the particles much freer, guaranteeing higher speed. This means that in a cloud the major number of collisions and so the biggest droplets are in the upper part [19].

This collision-coalescence process take place with particles of the size bigger than 40 μm . It is difficult to understand the mechanism behind the growth of the droplets in the size range 15–40 μm where both the diffusion-condensation process and the collection process are ineffective [20].

2.3 Clouds structure

Water concentration within a typical cloud (cumulus, stratocumulus) span from *10-100 droplets/cm³* for small-sized droplets to *1 droplet/cm³* with *radii >250 μm* . Therefore, as mean radius increases, water concentration decreases, consequently spectrum peaks move to the right and downwards, broadening the spectrum shape. In parallel the higher is water concentration, the narrower is the spectrum and the smaller is the mean size of drops [14].

It is necessary now to focus on the shape of the droplets' spectrum as a function of the location within the cloud. If a cumulus is crossed vertically, it can be observed how the concentration of the droplets varies trough the vertical and horizontal extension of the cloud; all those information were taken thanks to aircraft measurements.

- Vertical variability, as shown in figure 2.8 cumulus clouds led us to observe that changes in concentration and size are not significant going up through the cloud

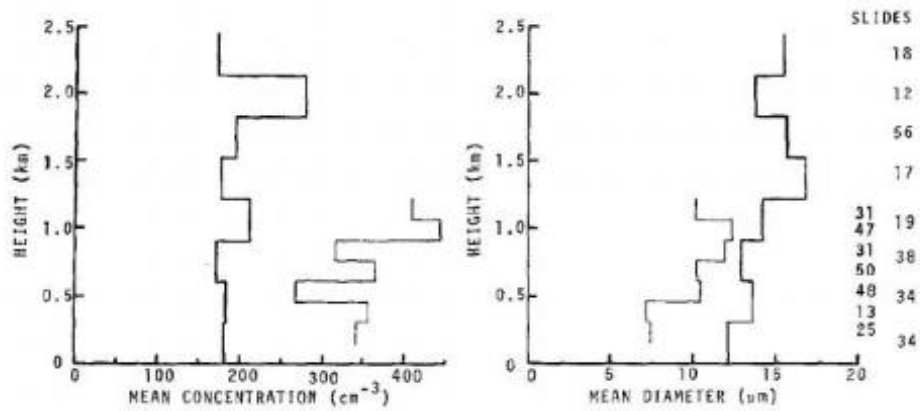


Figure 2.8: mean diameter and droplets concentration variation with height in cumulus cloud [21]

However, it is present an increase in the range of large droplets that have low concentration. Consequently, as shown in figure 2.9, is visible a slight widening of the spectrum as the measurements were taken towards the cloud top, as well as an increase in frequency of bimodal distribution [21]

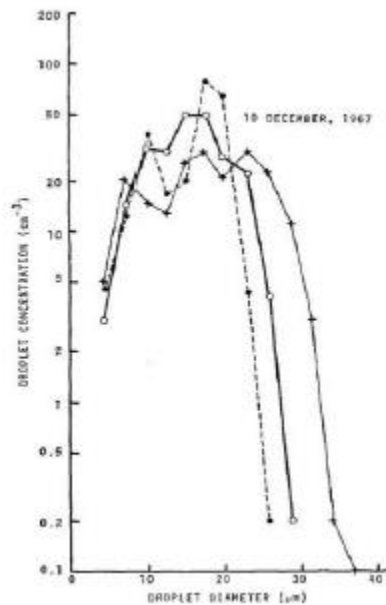


Figure 2.9: three average spectra for different heights above the cloud base, it is visible that toward the cloud's top the spectrum is wider in the range of large droplets that have a lower concentration in the lower cloud' layers [21]

- Horizontal variability: from the following figure 2.10 . Can be seen wide regions of homogeneous droplets distribution (a), interrupted by micro-zones where droplets concentration drops almost to zero (b). There are also interfaces between cloud and still air (c and d), the growth of number of droplets is sudden [22] [23].

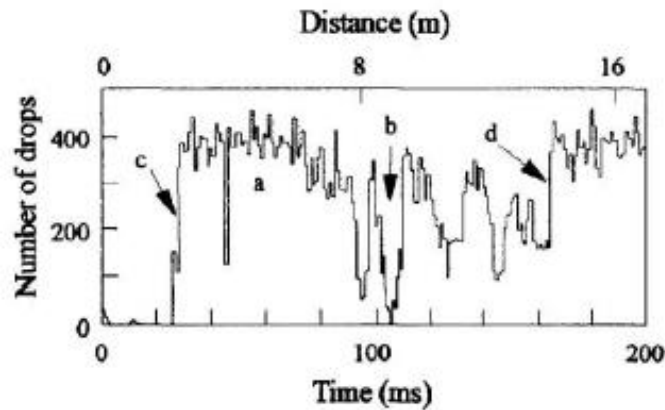


Figure 2.10: droplets concentration measured at 1000 Hz during a flight through a small cloud, it is visible a greater variability respect to the vertical height variation [22]

2.4 Turbulence

Turbulence in fluid motion causes sudden variation in pressure and velocity because of intense fluctuation. It is still nowadays a source of uncertainty due to its nonlinear nature, indeed numerical simulations, experiments and in-situ measurements haven't managed to describe it properly yet.

A turbulent flow depends on time and space and its dynamic involves different scales, from the larger ones, those of the mean flow, to the smaller ones, those involved in the viscous energy dissipation. Large scale motions take out energy from the mean flow and pass it through an '*energy cascade*' to the small scales. The smallest scale is the *Kolmogorov scale* and is the one where dissipation takes energy out of the system. The *energy cascade* ends at sufficient small scale where the viscous dissipation becomes the leading phenomenon of the system, the kinetic energy supplied by the mean-flow motion is converted directly in to heat due to viscous dissipation. The magnitude of the smallest scale it is related to the Reynolds number, as the Reynolds increases, the size of the *Kolmogorov scale* decreases. Large-

scale structures and eddies are strongly dependent on the boundary conditions, on the counter side small-scale structures have universal proprieties.

Regarding the atmospheric system, clouds are natural phenomena that involve fluctuations, non-stationary and inhomogeneous processes. A lot of turbulence is present inside clouds much more than outside them, that implies the presence of many temporal and spatial scales. The biggest scale is around 100 m, and the smallest is around 1mm. In clouds the typical Reynolds number is much higher than the critical one that leads the turbulent transition [24].

Inside clouds drops are transported and dispersed by turbulent large-scale eddies, simultaneously at drops-scale droplets modify the local system through variation of mass (condensation and evaporation), of momentum (viscous drag) and energy (latent heat). For instance, the phase transformation between water and vapor in the air and the liquid water in droplets introduces bulk buoyancy effects that drive cloud-scale motions. The extreme density contrast between the droplet and the air implies a significant (at the microscale) droplet inertia and terminal velocity, making the droplet-turbulence interaction nonlocal and multiscale in nature [25].

Has been observed that typical turbulent dissipation rate *epsilon* is around $10^{-1} \text{ m}^2/\text{s}^3$ in stratocumulus clouds, $10^{-3} \text{ m}^2/\text{s}^3$ in small cumulus clouds, and a mostly variable range of 10^{-4} to $10^{-2} \text{ m}^2/\text{s}^3$ in precipitating clouds. [24] [26]

However, this is a very variable and uncertain parameter, and it does not give further information about the big fluctuations in the local ε . The ε parameter seems to be dependent on the height, reaching its maximum value at the top of the cloud, that can be stated looking at the measurements made by [27] and [28]. Another reason why the dissipation rate is higher at the cloud top is that entrainment plays a key role in mixing external air with cloudy air. The phenomenon of entrainment will be explained better in the following chapters.

2.4.1 Turbulence and the development of drops

Despite the variability and uncertainty related to turbulence, studies and numerical simulations have stated that turbulence, at both large and small scales, plays a fundamental role in the rise of drops and the formation of mature-rain clouds. A paper shows that in systems like cumulus clouds, turbulence shorten the formation of drizzle drops by up to 40% in respect to the case of absence of turbulence [29].

Another paper shows that turbulent dissipation rate reaches $1000 \text{ cm}^2/\text{s}^3$, the conversion rate of cloud droplets in raindrops can improve by about 50% [30].

Turbulence plays an important role on both diffusional growth and on droplets collision. Regarding the diffusional growth, large-scale turbulent motions can move larger droplets from region where higher supersaturation enhances the growth of drops to region fewer active regions. In those regions larger droplets enhance further condensation and coalescence. Regarding the effects on turbulence on droplets collisions, it has been observed that turbulence produces large-scale accelerations that lead to droplets clustering and therefore to the increase of the collision rate [31].

Clustering is an important aspect of rain formation; it enhances the difference size between droplets and therefore the air flow is characterized with droplets with different inertia that move diversly [18].

Turbulence plays a fundamental role also at small-scale, indeed smaller eddies enhance the motion from large eddies to others, this process is called *large eddy hopping* [16].

2.4.2 Droplets motion

There are two non-dimensional parameters that help to understand how drops move in clouds: Stokes number S_t and the non-dimensional terminal velocity S_v .

Stokes number is defined as

$$S_t = \tau_d / \vartheta$$

Where τ_d is the *inertial droplet response time* which is the characteristic time a particle takes to react to changes in flow, $\tau_d = \beta d^2 / (18 \nu)$, where *beta* is $\beta = \rho_d / \rho$, the ratio between the density of the droplet and the air, d is the droplet diameter, ν is the kinematic viscosity of the air, ϑ is the Kolmogorogov timescale, defined as $\vartheta = \left(\frac{\nu}{\epsilon}\right)^{1/2}$, where ν again is the kinematic viscosity of the air.

If $S_t \gg 1$, particles react very slowly to flow changes, while with $S_t \ll 1$ they follow the flow exactly. It is expected that preferential concentration results when $S_t \approx 1$ [32].

The Stokes number gives details about the relative speed between particles, when:

- $S_t \approx 1$ there will be a maximum relative velocity
- $S_t \gg 1$ the inertia of the droplets creates differences between the motion of droplets and that of the mean flow

- $S_t \ll 1$ droplets follow the motion of the mean flow, indeed the difference in relative velocity between the droplets and the flow is negligible.

The other important parameter is the non-dimensional terminal velocity S_v

$$S_v = \frac{v_t}{v_\eta} = g \frac{\tau_d}{v_\eta}$$

Where v_t is the droplet terminal velocity and v_η is the Kolmogorov velocity scale. The non-dimensional terminal velocity helps to understand the time of interaction between a droplet and a Kolmogorov scale dimension eddy. If $S_v \gg 1$ droplets interact slowly with eddies, the opposite happens when $S_v \ll 1$.

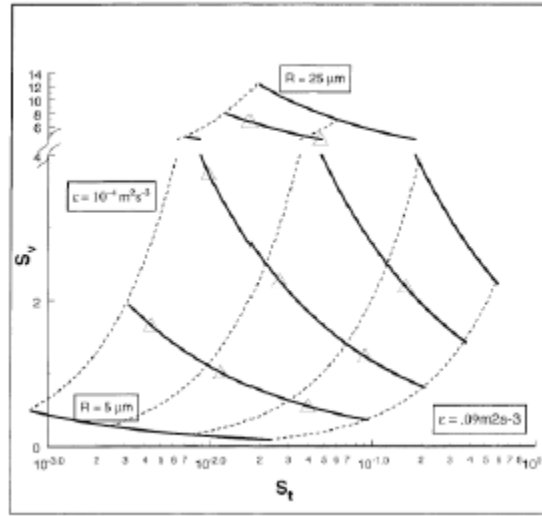


Figure 2.11: velocity ratio-Stokes number (S_v - S_t) diagram for typical sizes of cloud droplets for an appropriate range of eddy dissipation rates. The dashed lines are for constant dissipation rates while solid lines are for constant radii [33]

The motion of a small droplet in a turbulent flow is described by the following equation [33]

$$\frac{dv_i}{dt} = \frac{u_i - v_i}{\tau_d} + g_i$$

Where v_i is the droplet velocity in the i direction, u_i is the flow velocity, g_i is the acceleration and τ_d is the inertial droplet response time.

When $S_t \ll 1$ the equation becomes

$$v_i \approx u_i + \tau_d g_i - \tau_d \alpha_i$$

Where α_i represents the Lagrangian acceleration of the fluid at the droplets' location. Observing the previous simplified equation, it can be stated that drops move with the air around themselves with a

relative motion caused by gravitational settling and inertial response of droplets to mean flow accelerations [33].

2.5 Entrainment

Entrainment is an atmospheric phenomenon that involves turbulent streams flowing by another one with different density. Fluid particles that come across the turbulent region irreversibly acquire vorticity and start to move along with the turbulent stream. The way in which entrainment occurs within a cloud could have important implications for the nature of the mixing process and the measure of spectrum widening that entrainment normally generates [34].

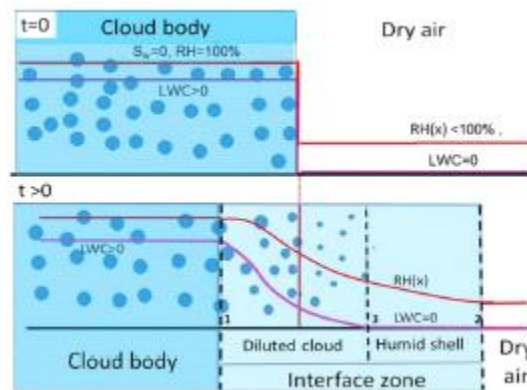


Figure 2.12: Conceptual scheme of zones in the vicinity of the cloud–dry air interface (top) at $t=0$ and (bottom) for the developed interface zone. The initially sharp cloud–air interface is shown by red line in the top panel. Zone between vertical lines 1 and 3 is the dilution cloud zone. Zone between lines 3 and 2 is the humid shell [34]

2.5.1 Entrainment's mechanism

The mechanism of entrainment occurs through three main steps [34]:

- Engulfment or nibbling of dry air inside the cloud through the action of turbulence.
- Stirring, the formation of mostly separate clean air and cloudy air filaments that reach the Kolmogorogov scale

- The filaments gradually become increasingly smaller, until they reach sizes in the order of η , a measure to which they become homogenized.

The term engulfment is often used to describe the phenomenon when it occurs due to large scale turbulent motions, while nibbling is used for small scale. Simulations and laboratory experiments have shown that nibbling is a more often dominant process than engulfment, whereby it appears that molecular diffusion could be the dominant process. This is true if the level of instability resulting from turbulence does not increase significantly, because then nibbling would seem to become negligible [35]. Environmental conditions and the cloud type both play a fundamental role in the entrainment process. In isolated cumulus, dry air entrainment causes a strong cloud dilution compared to its effects on a stratocumulus. For cumulus clouds the nature of the entrainment is still subject of debate. Indeed, [35] states that vertical entrainment, through the penetrative downdraught into the cloud top, was the main dilution mechanism in cumulus clouds, on the counter side [36] argues that cloud top entrainment, considering the small descending mass fluxes, cannot cause the observed dilution in cumulus clouds. Stratocumulus dynamics is very different from the one of isolated cumulus clouds therefore the entrainment processes that take place are different. Stratocumulus forms at the stably stratified transition layer (temperature inversion or density interface) which separates the shallow, cool and moist thermal boundary layer and the much warmer and drier subsiding atmosphere, capping the mixing layer. In this case the entrainment of warm and dry air from above occurs at the cloud top interface, thanks to the convective turbulence, driven by infrared radiative cooling at the cloud top, impacting the cloud top interface [37].

2.5.2 Entrainment's consequences

The first main consequence of entrainment process is the reduction of the liquid water content inside the clouds which influence the evolution of clouds droplets and rain formation.

Entrainment plays a key role in CNN activation above the cloud base: clear supersaturated water interacts with swirling structures associated with instability at the interface between the cloud and the environment [38].

As a result, it penetrates inside the cloud, raising the level of supersaturation and thus promoting the activation of CCN. [21].

Entrainment in shallow cumuli plays an important role in additional activation of entrained CCN: clear air supersaturated interacts with swirling structures associated with instability at the interface between the cloud and the environment. As a result, it penetrates inside the cloud, raising the level of supersaturation and thus promoting the activation of CCN [38].

It can now be introduced the Damköhler number

$$Da = \tau_r / \tau_s$$

Where τ_r is the characteristic time of a turbulent vortex of radius r while τ_s is the characteristic time of a thermodynamic reaction related to the case under examination [18].

There are two different scenarios:

- $Da \gg 1$, turbulent fluctuations are slow compared to thermodynamic reactions and can be in some cases neglected. As for the entrainment, in this case we speak of inhomogeneous entrainment, because the typical evaporation caused by the phenomenon cannot act uniformly, so some droplets will evaporate while others will remain unchanged. In other words, droplets mixed with dry air will evaporate before being mixed in the cloud. Hence, filaments of air without droplets (which have evaporated) will remain inside the cloud until the air becomes over-saturated. The effect of this type of mixing is a decrease in the number of droplets, while the average size will remain unchanged, so the shape of the spectrum does not change. The fact that the concentration is lower leads to an increasing supersaturation and therefore could also enhance growth of the larger droplets [22].
- $Da \ll 1$, the opposite happens. In this case the evaporation rate is the same for all the droplets, so they will all evaporate, but slightly, so that the number of droplets does not decrease, but the average diameter of all of them decreases. In this case of homogeneous mixing, then we consider the instantaneous entrainment, so fast that it does not consider the horizontal variability that could be caused by evaporation the spectrum widens because the supersaturation decreases [22].

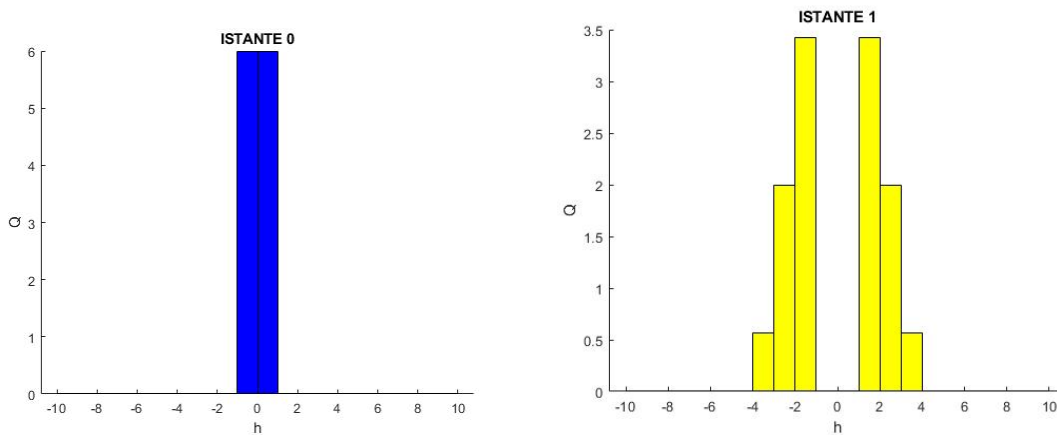
2.6 Richardson model of atmospheric diffusion and distance-neighbour graph

Lewis Fry Richardson published in 1926 a model for the dispersion of particles when turbulence is fully developed. The fundamental idea of this model is that the rate of diffusion increases with the distance apart. To have a general measure of the spread of a cluster of N marked molecules it can be imagined that the space considered is divided into cells with dimension h . Then it should be considered the relative distance between each particle from its point of view. For each nh , where n is an integer, it should be taken in consideration the number of pair-particles that see each other in that range in the variable $A_{n,n+1}$, $B_{n,n+1}$, $C_{n,n+1}$ etc and then sum up in the variable $Q_{n,n+1}$

$$Q_{n,n+1} = \frac{1}{N} (A_{n,n+1} + B_{n,n+1} + C_{n,n+1} + \text{etc})$$

It is therefore possible to obtain values for $Q_{0,1}$, $Q_{1,2}$, $Q_{2,3}$ which are the numbers of molecules per length classified according to their distances l from other molecules, these l distances lie in the range 0 to h , h to $2h$, $2h$ to $3h$ and so on. In order to have a graphic visualization of the diffusion it possible to draw a diagram in which the ordinate is the variable $Q_{n,n+1}$ and the abscissa is the length l . The length h should be chosen so that in the average $Q_{n,n+1}$ the space element shall contain a considerable number of molecules. [40]

The following diagrams represent at different instants the evolution of a cluster of 7 molecules and how Q varies respect to the distance l .



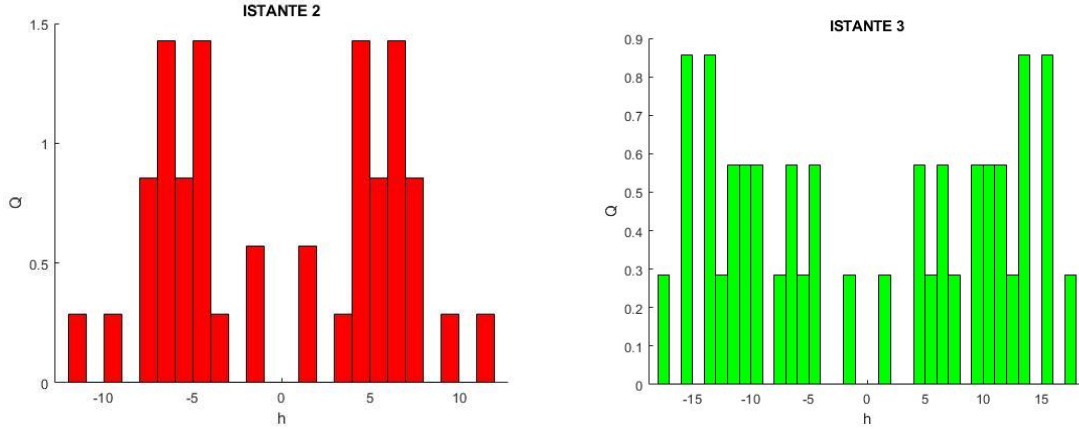


Figure 2.13: Evolution of the number of neighbor Q at increasing length l considering a population of 7 molecules for three different time instants- every second it is taken a shot image - respectively in figure a),b),c) and d). In the first image all the molecules see each other in the first $(0-l)h$ and Q has a peak, than the diffusional process begins and molecules spread out, when Q has a peak there is a cluster of molecules.

It is possible to notice that the $l-Q$ diagram is symmetric about the Q -axis and as diffusion proceeds the area under the curve is constant, indeed the curve flattens out as l increases. This behavior $l-Q$ curve leads to the fact that some function of l which attains a limit as $l \rightarrow \infty$ equal to that $l \rightarrow -\infty$ exists. Then, it is possible to say that Q must satisfy a differential equation as:

$$\frac{\partial Q}{\partial t} = \frac{\partial}{\partial l} \left\{ \begin{array}{l} \text{some function of } l \text{ wich attains} \\ \text{a limit as } l \rightarrow \infty \text{ equal to that} \\ \text{attained as } l \rightarrow -\infty \end{array} \right.$$

2.6.1 DNS model

Warm clouds are controlled by the tight interplay between radiative driving, turbulence, surface fluxes, latent heat release, and entrainment; large-scale analyses of atmospheric flows are fundamental in order to have an accurate representation of their dynamics. Among these phenomena the mixing and entrainment processes at the cloud top have been identified as fundamental to determine the internal structure of warm clouds, so that a clear and complete understanding of their physics is required, for this reason, a Direct Numerical Simulation (DNS) of the local transport through a clear air/cloud interface is

presented in figure 2.16 [61]. The complexity of the multi scale cloud dynamics becomes fully apparent at the cloud boundary where air, water vapor, and droplets and less humid air, interact in a situation where turbulence is highly intermittent and anisotropic. DNS, which resolve the turbulence down to the finest scales, can help to associate turbulence dynamics to a simplified cloud microphysics model that includes droplet formation, growth, and interaction. In particular, inside an atmospheric cloud, the shear-free mixing layer is considered a good model flow for the edges of a small portion of cloud and an adjacent clear air portion of equivalent volume at different turbulent intensity. Indeed, clouds are intrinsically non-steady, and their intrinsic anisotropy includes the small scales of the turbulence. The shear-free turbulent mixing layer is fundamentally simple because it is free of the turbulence production, this model is a typical situation of the life of clouds as the presence of a mean shear causes atmospheric clouds to quickly dissolve [61]. The starting condition models local mild unstable stratification in temperature and density; evaporation, condensation, collision and coalescence are phenomena included in the droplets' model. The analysis investigates the effect of transient anisotropic turbulence on both a monodisperse and a polydisperse population of water droplets initially randomly positioned in the cloud region. The schematic of the domain is presented in figure 2.14.

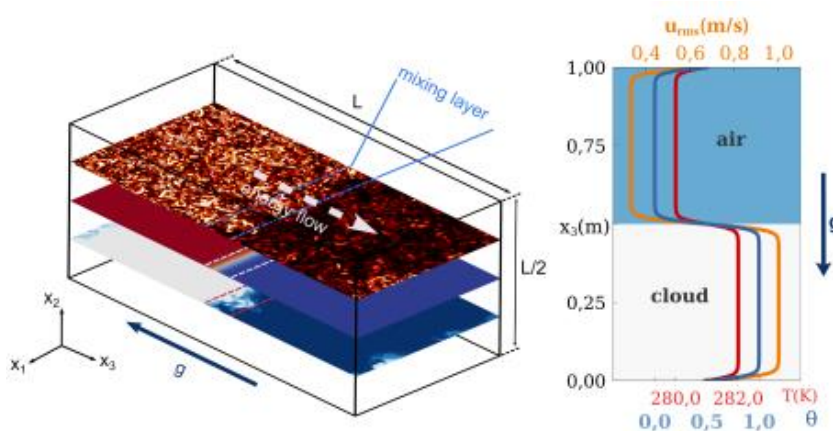


Figure 2.14: (a) Schematics of the simulation domain (left panel) and (b) of the initial profiles of the rms velocity (orange), temperature (red) and vapour content (blue) (right panel). In panel (a) the computational domain is represented as a parallelepiped composed of two adjacent cubes; subscripts 1 and 2 refer to the horizontal directions, subscript 3 indicates the vertical direction [61].

The governing equations are the incompressible Navier-Stokes ones, used with the Boussinesq approximation for both temperature and vapor density, and active scalar transport equations for the water vapor and thermal energy. The Boussinesq approximation allows one to take into account small perturbations of a parcel density of moist air due to local temperature and vapor density variation. This model is coupled to the vapor and temperature equations through their respective evaporation-condensation source terms. Inertial water droplets are represented via a Lagrangian approach, including Stokes drag and gravitational settling. This model is coupled to the vapor and temperature equations through their respective evaporation-condensation source terms. Code versions and releases could be found on the official Philofluid Research website

(<https://areweb.polito.it/ricerca/philofluid/software/95-turbulent-flows.html>).

The size of the computational domain is $0.512m \times 0.512m \times 1.024m$ and is discretized by using $512 \times 512 \times 1024$ grid points. Since the turbulence intensity and thus the dissipation rate, decay in time, the small scales, in particular the Kolmogorov scale, grow in time. This allows the grid size of $1mm$ to be well below the smallest scale of the system during most of the transient decay and nearly equal at the initial time.

In the simulation cloud droplets are assumed to be point particles. Therefore, they are always smaller than the grid size. The liquid water component is modeled as a Lagrangian ensemble of N point-like droplets. A collision is supposed to occur when the distance between droplet centers is equal or below to the sum of their radii. Collided particles coalesce, and the resultant particle has a volume equal to the sum of the collided particles and keeps as identity the smaller ID number. If the droplets radius becomes smaller than the critical value where the response time, the droplet is removed. The evolution of the drop is evaluated through condensation, evaporation and coalescence after collision. The growth by condensation/evaporation is modeled using the Köhler theory. Another aspect considered is the Kelvin effect: the curvature of the drop lowers the bonding strength between water molecules on the surface. Therefore, as the curvature increases and the radius decreases, the probability that water molecules leave the surface is higher. Furthermore, the atmosphere contains many other kinds of solid, or soft matter, or liquid particles. Some of these are hydrophilic and water soluble. The effect of soluble CNN on water evaporation rate is called the Raoult effect that is included in the model. Collisions are assumed to be completely inelastic; the mono-disperse initial distribution has particles of size $15\mu m$ and the multi-disperse distribution of droplets has a distribution of radii from $15\mu m$ to $30\mu m$ [61]. Droplets are initially placed in the cloud where the turbulent energy is higher. The initial spatial distribution is

random and uniform. The monodisperse distribution, a drop size selected distribution, presents a small number of collisions given the fact that equal drops do not collide unless the local spatial variation of the turbulent air velocity are sufficient to give neighbouring drops different velocities leading to collision. The other way around, inside a polydisperse drop size distribution, the collision rate is high because different inertial drops show a different motion relative to the air and this is even more so because of gravity. In the following table are presented the key simulation parameters and initial conditions [61].

Quantity	Symbol	Value	Unit
Domain size	$L_{1,2}^2 L_3$	0.152 ² 1.024	m ³
Domain discretization	$n_{1,2}^2 n_3$	152 ² 1024	-
Grid step	Δx	10 ⁻³	m
Initial rms velocity (cloud)	$u_{rms,1}$	0.11	ms ⁻¹
Initial integral scale	l_0	2.56 10 ⁻²	m
Initial dissipation rate (cloud)	ε_0	0.05	m ² /s ³
Initial energy ratio (cloud-clear air)	E_1/E_2	6.7	-
Initial Kolmogorov time (cloud)	$\tau_{\eta 0}$	1.74 10 ⁻²	s
Initial Kolmogorov length scale (cloud)	η_0	5.1 10 ⁻⁴	m
Initial eddy turnover time	$\tau_0 = 2l/(u_{rms,1} + u_{rms,2})$	0.35	s
Initial Reynolds number (cloud)	$Re_l = l u_{rms}/\nu$	196	-
Droplet response timescale (1μm, 30μm)	$\tau_d = 2\rho_v R/9\rho_0\nu$	4.410 ⁻⁴ , 1.310 ⁻²	s
Integration time step	$\Delta t = \frac{1}{20} \Delta x/u_{rms}$	4.64 10 ⁻⁴	s
Initial droplets number (monodisperse distr.)	N_{tot_mono}	8 10 ⁶	-
Initial droplets number (polydisperse distr.)	N_{tot_poly}	10 ⁷	-
Initial droplets radius (monodisperse distr.)	r_{0_mono}	15	μm
Initial droplets radius (polydisperse distr.)	r_{0_poly}	0.6 - 30	μm

Table 2.1: key simulation parameters and initial conditions for the DNS analysis.

Using the DNS simulation of a physical domain in which are present 292 molecules that evolve over a period of 35scale time instants it is possible to have a wider point of view of the Richardson model because of the bigger and more realistic cluster. In figure 2.16 is possible to evaluate the evolution of Q

over l over time, as in figure 2.18.a the area under curve tends to flatten out over time along the l -axis and during time the diffusion process creates clusters of molecules that are represented by the highest values of Q . In figures 2.18.a and 2.18.b it is possible to have different visualization of the same process. In figure *a* it is possible to evaluate Q over time for the first 5 l ranges: Q has a peak at instant 0 as all molecules are released from a known point of the physical domain considered as the origin, so that all see each other in the range of $(0-1)l$. As the molecules are free to expand in the domain over time they spread out and Q tends to decrease in the low ranges of l , when evaluating 3D model (Figure 2.17) it possible to notice that the new available direction allows droplets to spread out quicker. On the counter side at instant 0 high values of l report none values of Q (as all molecules are in the origin) but over time Q grows where there are cluster of molecules in the domain. In figure 2.18 a and b is reported the curve of $\frac{\partial Q}{\partial t}$ over time and as a direct consequence of the previous considerations for low l -ranges $\frac{\partial Q}{\partial t}$ tends to initially grow and then decrease over time, oppositely for high values of l $\frac{\partial Q}{\partial t}$ grows over time reaching its peak, or peaks, where there are molecules' clusters.

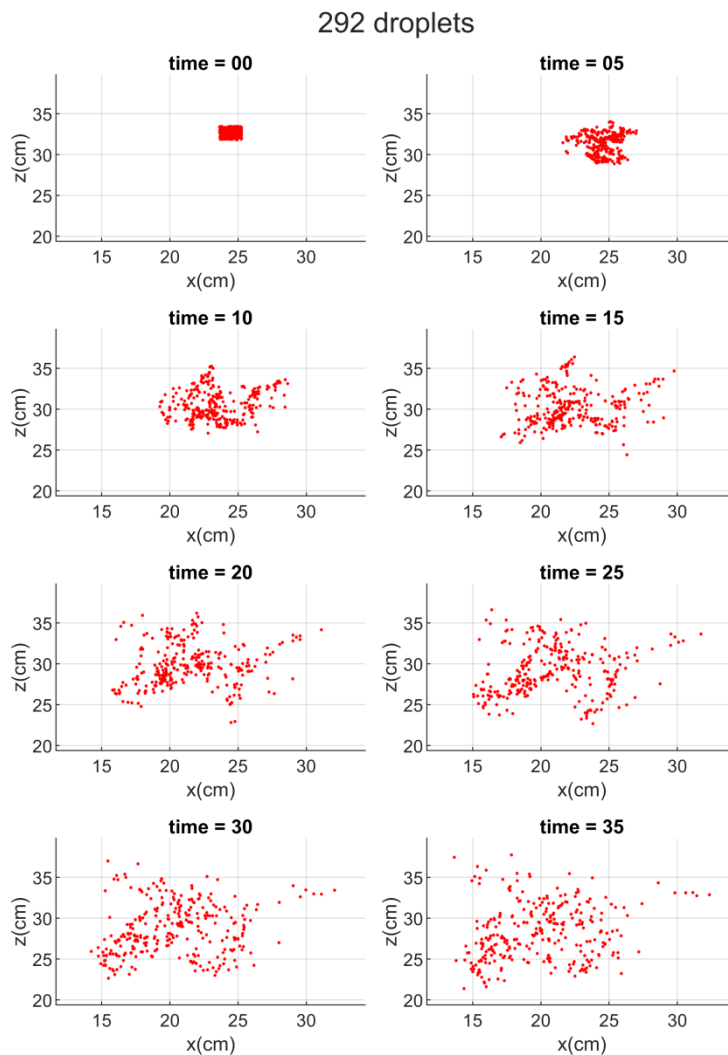


Figure 2.15: Droplets' dispersion over timescale instances (the timescale values are defined in table 2.1), which is defined respect to the dimension of the integral scale. It is visible how the molecules spread out in the domain, it is possible to have a quantification of the bigger clusters in figure 2.16 and 2.17 using the quantity Q .

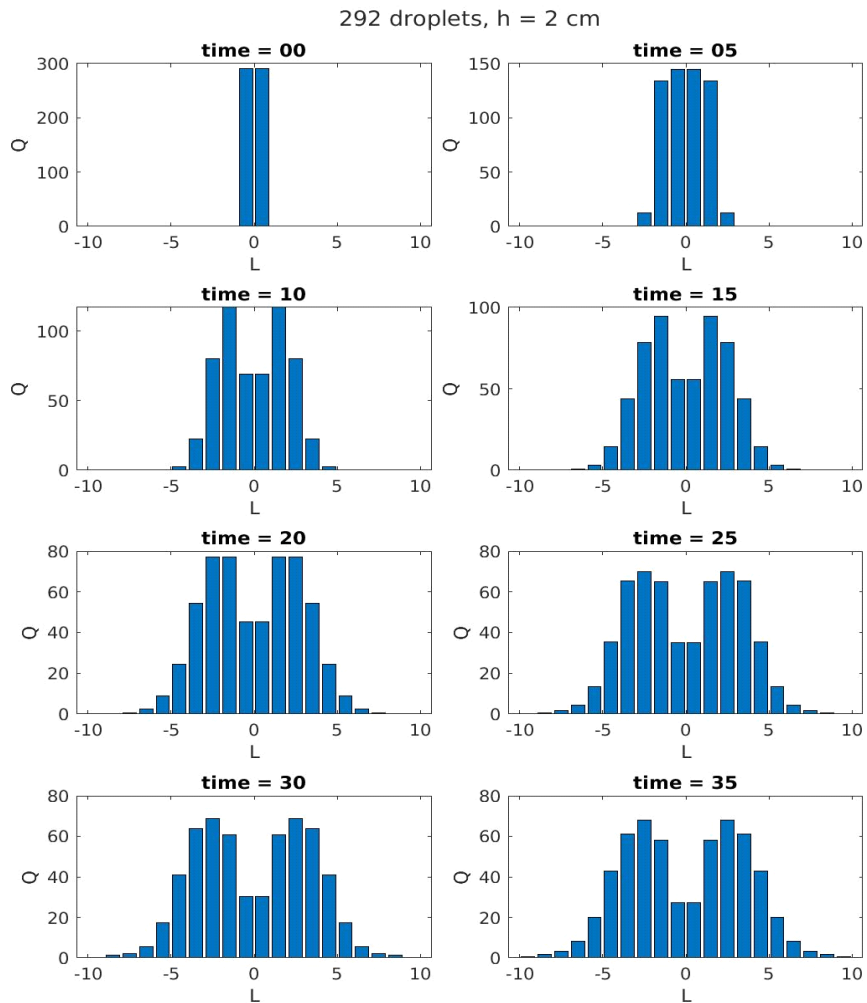


Figure 2.16: l - Q 2D diagram over the timescale specified in table 2.1. Starting from the initial time where the molecules are all close together and Q has a peak in the first length interval, the molecules spread out and the quantity Q indicates how many molecules see each other in the specific space range $(n, n-1)h$. When Q has a peak means that there is a cluster of molecules in that $(n, n-1)h$ interval.

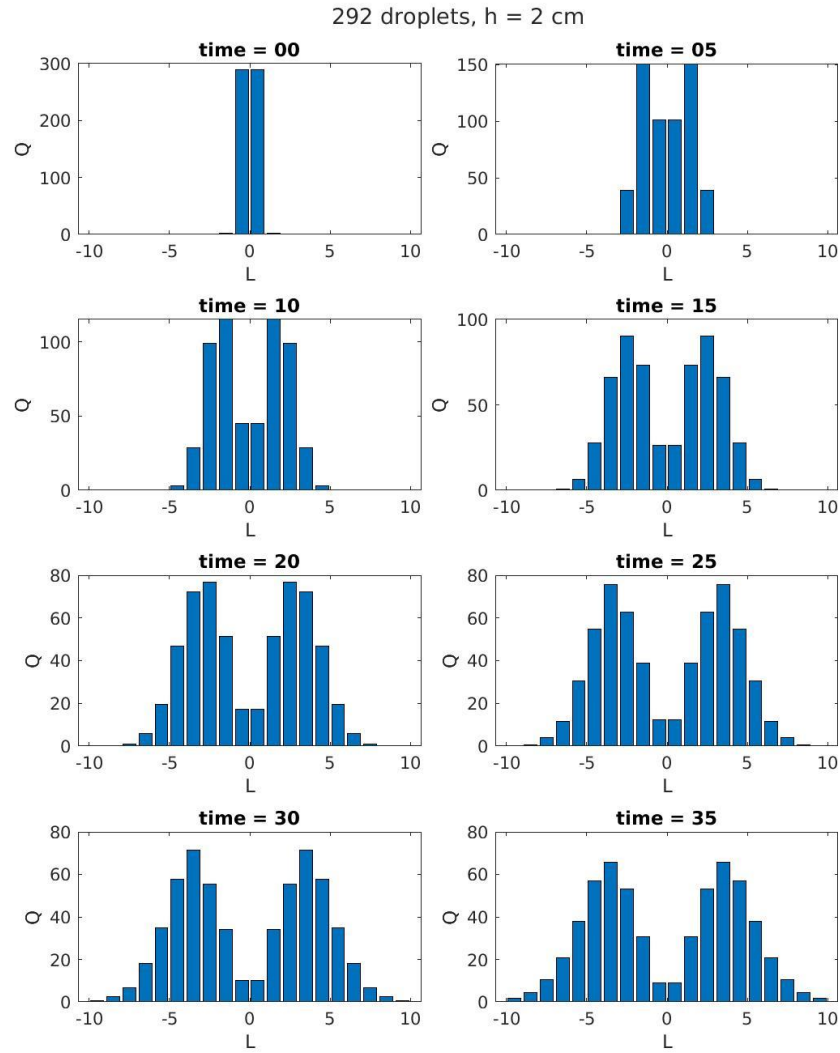


Figure 2.17: l - Q 3D diagram over the timescale specified in table 2.1. Starting from the initial time where the molecules are all close together and Q has a peak in the first length interval, the molecules spread out and the quantity Q indicates how many molecules see each other in the specific space range $(n-l, n)h$. When Q has a peak means that there is a cluster of molecules in that $(n-l, n)h$ interval. Respect to figure 2.16, it is possible to notice that Q in the $(0, l)h$ range lowers more quickly over time, that is because the third dimension gives more physical space to the domain considered.

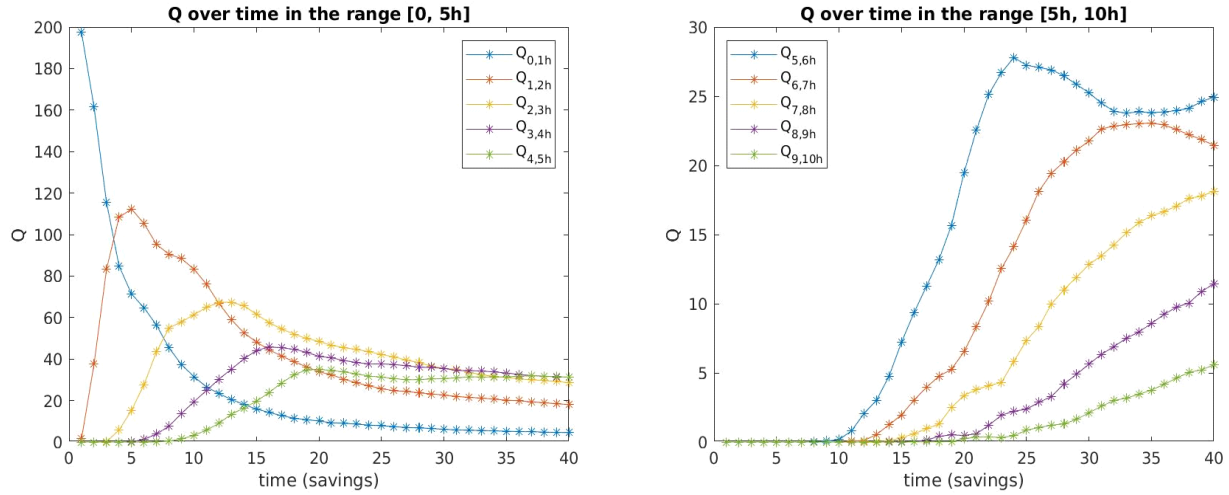


Figure 2.18: (a) Q over time for the five h intervals; it is possible to evaluate the same data presented in figure 2.17 in a more quantitative way. Q for $(0,1)h$ interval starts from a peak and decreases immediately, Q for $(1,2)h$ interval starts from a low value and reaches a peak over time. As $(n-1,n)h$ increases the peak of Q tends to move further in time, physically this is because particles spread out in the domain and they tend to occupy region of space further from the starting point. As $(n-1,n)h$ increases the peak reach lower values, this is another aspect of the same process: as particles get further from each other they will see less particles in the $(n-1,n)h$ considered. Focusing on figure (b) it is visible the trend of Q over time for the 5-10h intervals, that shows the same trend already described. In particular Q for the $(9,10)h$ interval does not even show a peak in 40 scalar time instances.

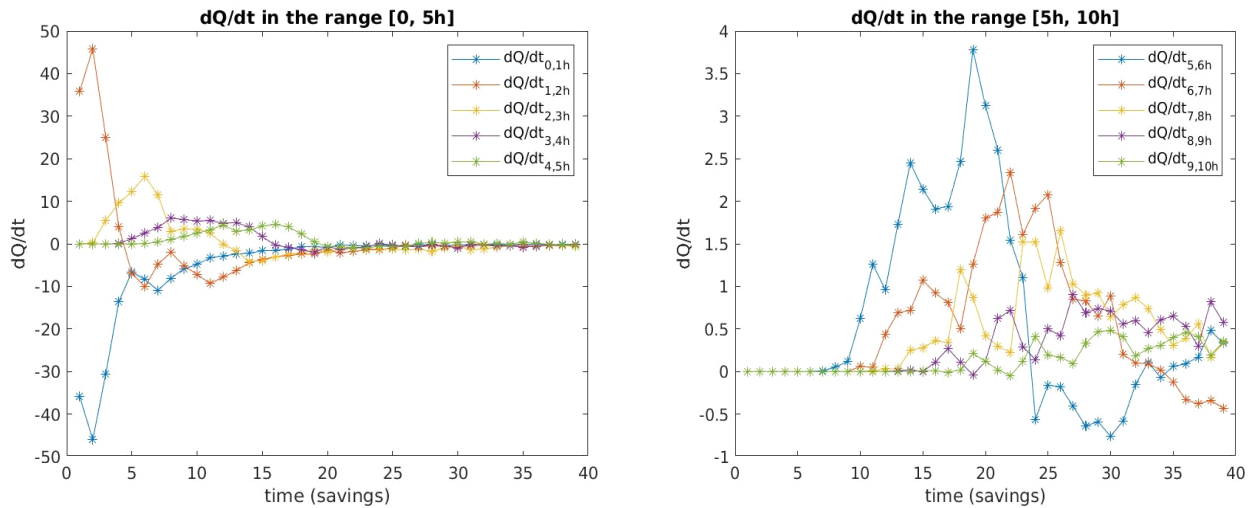


Figure 2.19: (a) dQ/dt over time for the first $0h-5h$ intervals: the variation of the quantity Q over time is related to the dispersion of particles in the domain, initially there is the greatest variation of Q as particles spread out from the starting point where were all close one to each other. As $(n-1,n)h$ increases the peak of Q tends to move further in time and the same happens to the highest value of dQ/dt , which at the same time also reaches lower values. In figure (b) it is shown the trend of dQ/dt over time for the 5h-10h intervals.

Chapter 3

The radiosonde

As already mentioned in the previous chapter, clouds' dynamics and turbulence are complex phenomena that still nowadays remain challenging aspects for weather forecasting and climate understanding, indeed they are related to independent natural processes at micro and macro scale. Clouds are considered a main challenge for scientific understanding and modeling, since the available methods are not yet able to characterize the entire cloud system and related interactions across scales. In situ measurements have been developed in order to better understand the how the small-scales turbulence influence the formation and growth of clouds. One of the possibilities to develop an in-field cloud Lagrangian dataset is to create ultra-light radioprobes capable of moving along the mean flow [41].

Nonlinear dynamical processes of vortex stretching, entrainment, and mixing greatly influence the nucleation of water droplets and associated evaporation-condensation and collision-coalescence [18].

Investigation methods include remote sensing by means of radars and lidars [59] [42], in situ observations including manned and unmanned airborne platforms (airplanes, helicopters, tethered lifted systems, etc.) [26] [43], laboratory experiments in wind tunnels and climate chambers [44] [45], and numerical simulation experiments carried out via Navier–Stokes direct numerical simulation of small portion of clouds [46] [47].

During the proposal writing of a European Horizon 2020 Marie Skłodowska Curie project (H2020 MSCA ITN ETN COMPLETE, GA 675675: Innovative Training Network on Cloud-MicroPhysics-Turbulence-Telemetry [48]) was suggested to use ultralight battery-powered radiosondes with radio transmitting capabilities carried in the atmosphere by a balloon filled with helium [49].

The mini radio probes are used to passively track turbulent fluctuations of air velocity, water vapor, and droplets concentration, temperature and pressure in warm clouds and surrounding ambient air according to the Lagrangian description [50] of turbulent dispersion, as proposed by Richardson in 1926 [40] [51].

The main goal of the COMPLETE (Cloud MicroPhysics Turbulence Telemetry) [52] Horizon 2020 project is to build up an in-cloud Lagrangian database and to create a multidisciplinary system able to extend current knowledge about non-linear multiscale natural phenomena within clouds.

One of the main tools with which COMPLETE intends to achieve its goal are insitu experiments, using an innovative light, floating, economical, biodegradable mini-radio probe. To achieve its main the probe must attain 3 important aspects:

- Floating on an isopycnic surface at a chosen altitude of about 1000m for a time spanning from the inner turbulence (scale of minutes) to the extension of cloud lifetime (few days), using a balloon filled with helium.
- Acquiring atmospheric data (pressure, temperature, humidity) and location data through the employment of sensors.
- Processing and transmitting the acquired data to a ground station using a mini antenna.

Atmospheric data will be captured through pressure, temperature and humidity sensor, in addition to movement sensors (accelerometer), which will capture data at regularly scheduled intervals [53]. Finally, the data will then be interpreted, processed, saved and transmitted through a micro-antenna to a ground receiver [54].

3.1 Ultralight radiosonde system Architecture and Design Methodology

These compact light-weighted devices with a maximum target weight of 20g and diameter of 30cm are designed to float at altitudes between 1–2 km and be alive for approximately 1h. The radioprobes are capable of passively tracking small-scale turbulence fluctuations inside warm clouds and surrounding air since they can be considered as markers in a Lagrangian description of the airflow. Each device must include sensors to measure velocity, acceleration, position, pressure, temperature, and humidity fluctuations inside warm clouds. According to the environmental conditions that can be found inside real clouds, the operational requirements for the radioprobe sensors can be summarized as follows: external temperature, ranging from 0 to +30 °C; external relative humidity (RH): ranging from 0 to 100% RH; external pressure: ranging from 400 to 1100 mbar; trajectory: +/-100 mm accuracy; and air-flow fluctuation: up to 5–6 m/s inside a cloud. The data collected during the flight must be sent wirelessly to a

data-acquiring system on earth whilst the device is alive. For this purpose, a transmission technology able to reach relatively long distances without consuming much power is required. In order to enable them to float, the radioprobe electronics are housed inside 30 cm-diameter balloons made of biodegradable materials that are filled with helium to reach a buoyancy force equal to the system weight. In the following image is summarized the system architecture:

- (1) the bio balloon-wrapped radioprobe
- (2) the base station, which receive, store and pass this information to the processing machine
- (3) the processing machine, which is used as for database management, filtering, and visualization

[41]

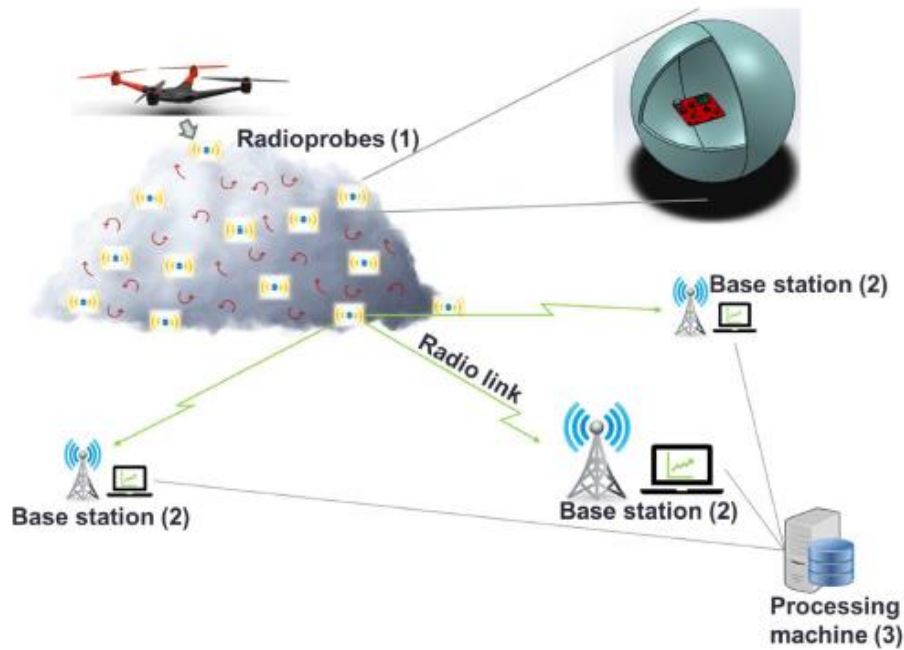


Figure 3.1: Scheme of the working principle and the radio-probe structure [41]

3.2 PCB structure

The block diagram of the radioprobe is illustrated in Figure 3.2, where the system is represented by its several functional units: (1) a data-processing and control unit, (2) a radio communication system, (3) a temperature, pressure, and humidity sensor stage, (4) a positioning and tracking sensor stage, and (5) a power supply unit.

The printed circuit board (PCB) realization of the radioprobe is displayed in Figure 3.3.

All the electronics are assembled on both sides of a two-layer FR4 substrate with surface mount technology (SMD) components. It is a 50 mm x 50 mm rectangular structure with a thickness of 0.8 mm and weight of 7 g (without the battery).

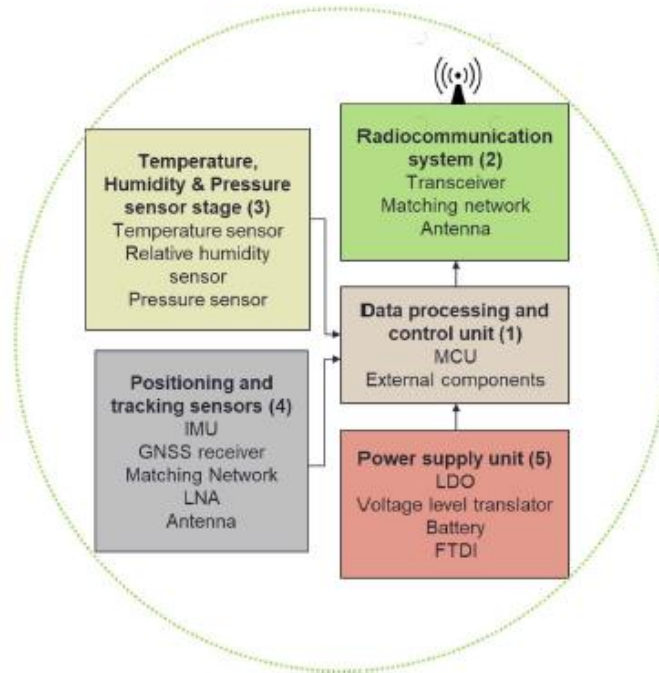


Figure 3.2: Block diagram of radioprobe system [41]

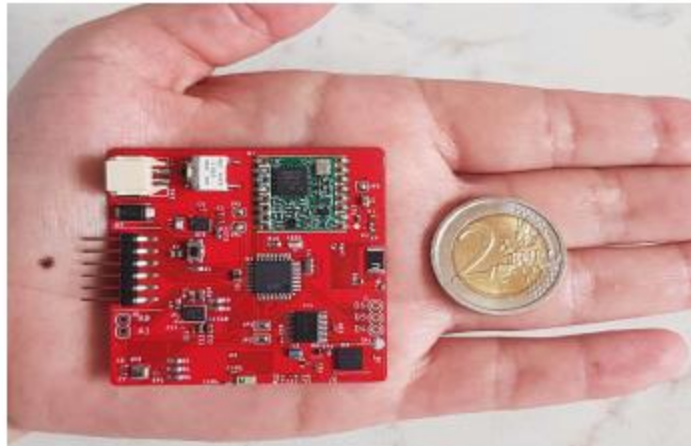


Figure 3.3: PCB implementation of the radioprobe

The PCB has [55][56]:

- *temperature sensors* with an operational range from -40°C to $+85^{\circ}\text{C}$ and a resolution of 0.01°C
- *Humidity sensors* with a range of 0% to 100% with an absolute accuracy tolerance of $\pm 3\%$ and a resolution of 0.008%
- *Pressure sensors* have a range from 300 hPa to 1100 hPa and a resolution of 0.18 Pa
- *Trajectory sensors* have an accuracy of about ± 100 mm and a frequency rate smaller than 10 Hz

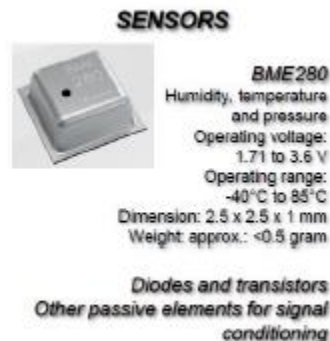


Figure 3.4: Humidity, temperature and pressure sensors specifics

The sampling period for pressure, temperature and humidity is 2s, while the period for capturing trajectory is chosen to be 0.1 s. To realize velocity and acceleration estimation, the chosen approach was radio signals combined with position estimation techniques to localize the target objects [55].

The energy necessary for the correct function of the radiosonde is provided by a battery at *Lithium Mental Oxide (LMO)* and by pulse current capacity of 3.75 A. The battery is chosen to be small and

lightweight; its dimension is: 23 mm of height, 5.4 mm of diameter, nominal voltage of 4V and nominal capacity of 125 mAh. It can be supposed that the consumption would be of 50 mAh without GPS and 100 mAh using GPS.

The computational module of the radioprobe is a CPU (CMOS 8-bit microcontroller A Tmega 328). It has 32 pins in a thin quad flat pack with compact dimensions and weight (9 mm x 9 mm x 1mm and 70 mg). Inside this unit the data sent by the sensors are interpreted, processed, saved and sent through the transmission module to the ground using a small antenna on the PCB. The sensors are kept in a sleep mode until they perform a measure, in this way power consumption is reduced.

DATA ACQUISITION AND CONTROL



Figure 3.5: ATmega 328 microcontroller specifics

The radio communication system is provided by a ceramic omni-directional antenna to transmit data to the receiver using radiofrequency signal. Information will be sent from the probe to a ground receiver, using frequency bands around 350 MHz or 169 MHz. Thanks to the good propagation link and the low attenuation the probe can be monitored at lower power during the entire fight through warm clouds. The signal is required to be received up to 20km, and the receiver has a sensitivity of -130dBm. Each probe must transmit at a power of at least -30 dB [57]. Due to the required criteria of the artificial floating probes, LoRa communication technology has been adopted. LoRa is a chirp spread spectrum (CSS) modulation technique, which encodes information in linearly increasing chirps [39].

TRANSMISSION SYSTEM



TRANSMISSION SYSTEM

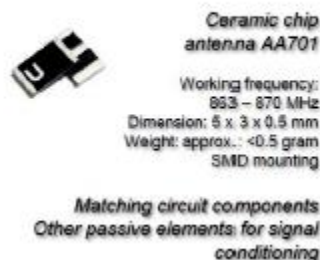


Figure 3.6: components of transmission system: LoRa transceiver and micro antenna

The positioning and motion tracking is executed as a post-processing task at the ground level and is obtained by sensor-fusion algorithms based on Kalman and orientation filters. The orientation filter is used to fuse data coming from an *inertial measurement unit* IMU, and the *Kalman filter* exploits the output of the orientation filter and fuses it with the data coming from a *Global Navigation Satellite System* (GNSS) receiver. The IMU used for this block is the nine-axis inertial module device LSM9DS1 that combines a three-axis digital linear acceleration sensor, a three-axis digital angular rate sensor and a three-axis digital magnetic sensor, all in a single package, the LGA package, of dimensions $3.5\text{ mm} \times 3\text{ mm} \times 1.0\text{ mm}$, requires a supply voltage in the range from 1.9 to 3.6 V. The GNSS receiver unit used in this block is a professional ultrasmall, super-low power system-in-package (SiP) ZOE-M8B module that offers a super-efficient (Super-E) mode option for improving the power consumption. It comes in an advanced soldered land grid array (S-LGA) package of dimensions $4.5\text{ mm} \times 4.5\text{ mm} \times 1.0\text{ mm}$, requires a supply voltage in the range from 1.71 to 1.89V [41].

In the following table are summarized the parameters measured by the radioprobe

Physical quantity	Range	Sample rate	Device
Humidity	[0, 100] %	1Hz	BME280
Pressure	[300,1100] mbar	1Hz	BME280
Temperature	[-40, +85] °C	1Hz	BME280
Acceleration	[-16, +16] g	10-925 Hz	IMU, LSM9DS1
Angular velocity	[0,2000] dps	10-195 Hz	IMU, LSM9DS1
Magnetic field	[1, 16] gauss	1-80 Hz	IMU, LSM9DS1
Longitude	Degrees	1-10 Hz	GNSS, ZOE-M8B
Latitude	Degrees	1-10 Hz	GNSS, ZOE-M8B
Altitude	Meters	1-10 Hz	GNSS, ZOE-M8B
Velocity	[0,500] m/s	1 Hz	GNSS, ZOE-M8B

Table 3.1: Radioprobe's parameters

3.3 Balloon's material

In order to create a balloon that works correctly, the material used must be:

- *Not too elastic*, because the probe is designed to maintain its volume constant. This is necessary also to keep the height of the probe almost constant; in fact, if it is too elastic, the helium inside the balloon would expand without problems.
- *Hydrophobic*, if not, water droplets inside clouds would tend to adhere at the surface with the consequence of a change in weight terms. This requirement can be satisfied using special coatings on the surface of the balloon but keeping in mind that it would imply an alteration of the weight.
- *Impermeable to helium*, it is clear that the more *He* would leak out of the balloon, the more altitude of the probe would decrease.
- *Cheap*, in fact because of the fragility of the probe, the light weight and that the use of GPS is not guaranteed, probes will not be recoverable. Several radiosondes will be produced, so the material must be cheap and easy to find.
- *Biodegradable*, as discuss above, at the end of its life, the balloon will be dispersed in the environment. This makes it necessary to be biodegradable.
- The material must guarantee a determined *inertia of temperature and relative humidity* between the inside and outside of the balloon: the sensors will be placed inside the balloon, so they may result insulated from atmospheric conditions and transmit incorrect data. To prevent this problem, the material must ensure that the temperature range ΔT and relative humidity range ΔRH are sufficiently low, with short transition times [41].

After several tests, the materials that respect all the criteria mentioned above were Latex, Myral, PolyLactic Acid (PLA) and Mater-Bi.

The elastic capacity of the material was tested with classic tensile strength tests. The samples were cut into the standard dog bone shape, 25 mm in length, 3.98 mm in width with the thickness being that of the material ($30\text{ }\mu\text{m}$), and the straining rate was set at 1 mm min^{-1} .

To assess the hydrophobicity, the contact angle between a $5 \mu\text{l}$ drop of water deposited on the surface of the film was obtained, which is the angle between the direction of the solid-liquid tension and the direction of the liquid-gas tension, tangent to the external surface of a drop, with the vertex at the three-phase liquid-solid-steam point (Figure 3.6). As the figure shows, the higher the contact angle value, the more hydrophobic the material can be considered.

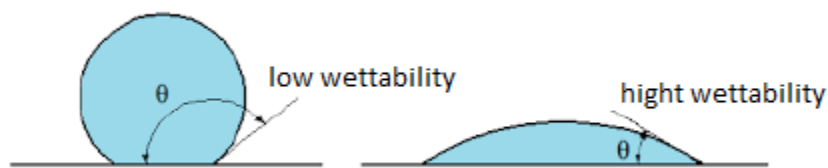


Figure 3.6: contact angle of a drop on a solid material, a) hydrophobic b) hydrophilic

To estimate helium permeability, balloons of the two materials were inflated with helium and placed on a scale, the velocity at which the weight of the balloons increase is directly connected with the extent of the helium loss.

Finally, to assess the difference in temperature and relative humidity between the inside and outside of the balloon, measurements were performed in the climatic chamber of INRIM, where values of ΔT and ΔRH can be chosen [58].

At the end the choice fell on Mater-bi, in fact, because of its characteristics, it turned out to be the most suitable material for our purpose. It is a bioplastic, very cheap bio-degradable, and most important easy to find, in fact classic shopping bags are made of Mater-Bi. If we add the possibility of spreading coating on the material, its characteristics improves further as shown in the table below (Table 3.1).

Material	Mean contact angle [°]
Latex	79
Myral	95
Mater Bi	89
Mater Bi+ carnauba wax	125
Mater Bi+ carnauba wax+ Pine Resin	73
Mater Bi+ carnauba wax+ SiO₂ NPs	140
PLA	83
PLA+ carnauba wax	126
PLA+ carnauba wax+ Pine Resin	81
PLA+ carnauba wax+ SiO₂ NPs	136

Table 3.2: contact angle for each material with difference coatings

In particular, the coating that includes silicon nanoparticles significantly increases the contact angle [58].

Chapter 4

Balloon

The creation of a proper balloon is fundamental to let the radio probe float on an isopycnic, that means at a constant density, level in the clouds following the Lagrangian motion of the particles, to let the radio probe collect data about pressure, humidity and temperature, and capture fluctuations due to the presence of turbulence. The balloon must provide stability to the probe and must follow the mean motion without interfering with its course. The balloon must follow the air stream without disturbing the turbulent structures, it must follow passively and faithfully the air flow. In order to achieve those qualities, it must be light, smallest as possible, spherical and biodegradable.

The best shape to obtain stability is the spherical one, the PCB with its battery should be placed in the center of the balloon to avoid oscillations that can alter the data measured by the sensors.

4.1 Preventive estimations

To estimate the proper size of the balloon it has been considered air density at sea level and helium density, indeed helium is the gas that will be used to blow the balloon. Moreover, it must be defined the weight of each part of the radiosonde so that the balloon would be able to lift the probe for at least one hour.

The first step is to fix the volume of the balloon, that will be filled with helium, indeed the probe must remain suspended in air for at least one hour.

The weight of the PCB system, that includes all sensors and the battery, must be balanced by the hydrostatic thrust provided by the helium inside the balloon's volume.

$$\text{Hydrostatic Thrust} = W_{tot}$$

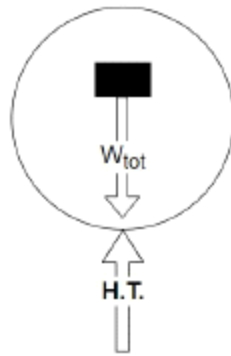


Figure 4.1: forces' equilibrium

The total weight of the system is given by:

$$W_{tot} = m_{tot} g$$

Because helium is a lighter fluid than external air it generates hydrostatic thrust

$$\text{Hydrostatic Thrust} = Vol g (\rho_{air} - \rho_{He})$$

The equilibrium

$$Vol g (\rho_{air} - \rho_{He}) = m_{tot} g$$

From the previous equation we can easily calculate the volume of helium needed

$$Vol = \frac{m_{tot}}{(\rho_{air} - \rho_{He})}$$

The density of a gas is dependent on the physical quantities that define the system in which the experiment is taking place. The link is given by the law of perfect gases

$$\rho = \frac{pM}{RT}$$

It is easier to refer the volume to the molecular weights of the two gasses air and helium, as they are independent on the external condition of the system; therefore

$$Vol = \frac{m_{tot}}{\rho_{air}(1 - M_{He}/M_{air})}$$

$M_{He} = 4.003$ and $M_{air} = 28.96$ are the molecular weights of helium and air.

It is important to keep in consideration the role of altitude, indeed temperature, pressure, density and dynamic viscosity vary with altitude; in the following table is shown the variation of air physical quantities with altitude within the troposphere (below 10km)

Z [m]	T [K]	P $\times 10^4$ [Pa]	ρ [kg/m ³]	μ $\times 10^{-5}$ [kg/ms]
0	288	10.0	1.22	1.79
500	285	9.5	1.17	1.78
750	283	9.3	1.13	1.77
1000	282	9.0	1.11	1.76
1250	280	8.7	1.08	1.75
1500	278	8.5	1.06	1.74
2000	275	7.9	1.01	1.73
3000	269	7.0	0.90	1.70

Table 4.1: air physical quantities respect to altitude

Considering the balloon as a perfect sphere, its diameter can be calculated with the following equation

$$d = 2 \left(\frac{3 Vol}{4 \pi} \right)^{1/3}$$

4.2 Dimensions

In order to determine the dimensions of the balloon it is necessary to know the exact mass of the components of the probe. In the following table are presented the weights used for the future calculations.

Elements	Weights [g]
PCB	7.5
Outer case	8
Battery	9
Additional structures	2.5
Overall	27

Table 4.2: Weights of the components of the probe

As the weights of the components are defined, it is possible to evaluate the total weight of the probe

$$W_{tot} = M_{tot} g = 30.5 \text{ kg} * 9.81 \text{ m/s}^2 = 0.299 \text{ N}$$

As consequence the hydrostatic thrust is

$$\text{Hydrostatic Thrust} = W_{tot} = 0.299 \text{ N}$$

Considering air density at sea level $\rho_{air} = 1.225 \text{ kg/m}^3$, the volume of the balloon is

$$Vol = \frac{m_{tot}}{(\rho_{air} - \rho_{He})} = 0.0289 \text{ m}^3$$

Consequently, the diameter of the balloon is

$$d = 2 \left(\frac{3 Vol}{4 \pi} \right)^{1/3} = 0.3907 \text{ m}$$

4.3 Assembly

The aim is to create a balloon which is as spherical as possible without complicating the overall structure as Mater-Bi is a delicate material which does not tolerate many manual processes. This is the reason why the balloon must be composed by the least number of pieces, of welding spots and seams as they are critical points where the material's properties inevitably deteriorate.

An inlet at the bottom of the balloon is used to easily inflate helium in the balloon, the procedure is shown in detail in the following sections. During the first experiments the PCB was placed in the center of the balloon using a pocket of Mater-Bi soldered onto a band fixed at the two ends of the balloon. Then the experiments have showed that the data measured with the PCB inside the balloon were not precise as those measured with the PCB outside the balloon, for that reason in the following experiments the PCB was placed onto the inlet used to inflate helium.

4.3.1 Instrumentation

The tools used to build the balloons are presented below:

- Bags of Mater-Bi with thickness of about 30 μ m, available in any supermarket
- A surgical scalpel/cutter to obtain the exact shape from the sheets of material
- A ruler of about 50 cm
- A pen to draw the desired shape before cutting it, as the material is very delicate it is important to be careful not to cut the sheets with the pen.
- A hand wheel sealer with heated wheel connected to a handle (figure 5.2-5.2b)

- A Teflon tape to be applied on the heated wheel to prevent Mater-Bi from sticking to wheel itself
- A sheet of rubber/silicone to work on in order to not damage the working surface
- A 99% of pure helium tank to inflate the balloons

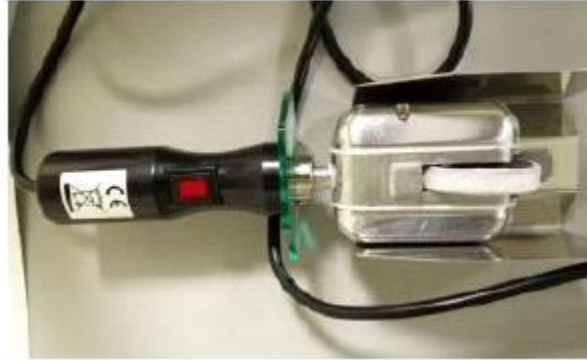


Figure 4.2: Hand wheel sealer



Figure 4.3: control knob to regulate the temperature of the heated wheel

4.3.2 Procedure

In order to create a balloon that has the desired characteristics summarized in table 4.3 the procedure to follow is explained step by step in this section

Volume	0.0289 m^3
Diameter	0.3907 m
circumference	1.2268 m

Table 4.3: desired characteristics

- Build 4 sheets of Mater-Bi material with the form shown in figure 4.4 and 1 with the shape shown in figure 4.5
- Cut the seams of the Mater-Bi bag and open it on the working table in order to have a rectangular sheet
- Using a pen and a ruler draw the shape shown in figure 4.4
- Using the scalpel/cutter cut the shape following the line just drawn as precisely as possible
- In order to waste less material as possible, the parts that are cut can be used to create the shape shown in figure 4.5 the procedure is the same: the line is created using a pen and then the scalpel/cutter is used to cut the shape just drawn

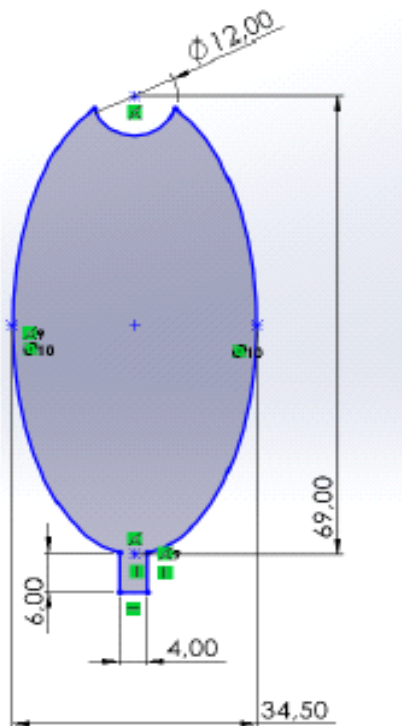


Figure 4.4: first shape with dimensions

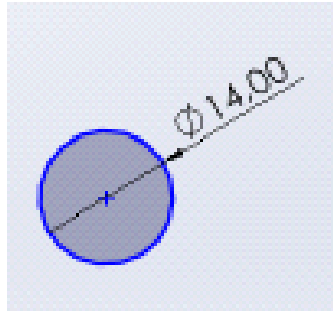


Figure 4.5: second shape with dimensions

- Plug the hand wheel sealer and use the small wheel on the potentiometer (figure 4.3) to set the correct temperature, that should be around 60-70°C. This tool requires about 15-20 minutes to reach the desired temperature, in order to not waste time, it is important to switch it on during the first step. As the wheel reaches the correct temperature for the experiment, it continues to overheat, therefore it is important at this stage to be careful at the wheel's temperature. If the wheel is too hot it will cut the Mater-Bi sheet, so it is best to switch of the hand wheel sealer for 3-4 minutes every 15-20 minutes and to do a quick test on a piece of waste material to be sure that the temperature is the correct one.
- As the wheel has the optimal temperature, two of the four shapes created in the first step are placed one onto each other and stick together. The hand wheel sealer must follow carefully the line drawn and the width of the weld part should be around 0.5 cm. As two of the shapes are stick another one is added, and the same procedure must be followed. In the end the last shape is stick to the main piece; it is important to leave a small part, close to the inlet, open, in this way the balloon will be easily turned, and the 0.5 cm sealed part will be placed inside the balloon. In figure 4.6 it is shown an inflated balloon and the 0.5 cm is clearly inside it, this characteristic gives much structural strength to the balloon when it is full of helium.



Figure 4.6: inflated balloon

- Fill slowly with helium until the balloon can push upwards. If the pressure inside the balloon is too high the welds can be damaged during the experiment.
- Close the inlet using a wire in order to not loose helium; if the knot is done properly the balloon can be reused in other experiments.

Chapter 5

Data obtained from experiments

In order to test the instrumentation developed and improve it, many experiments have been carried out. When a new prototype has been developed, those kinds of tests are necessary to improve its functioning and it also very important to repeat, over a period, the same tests several times in order to verify actual improvements.

5.1 INRiM experiment

At INRiM (*Istituto Nazionale di Ricerca Meterologica*) in Turin the radioprobe has been tested twice. The first test aimed at validating the COMPLETE system, the radioprobe, the biodegradable balloon, transmission and data acquisition. In a first moment the radioprobe was placed inside the balloon, in order not to compromise the motion of the balloon. Because the data measured by the mini radioprobe were not exact, the mini sonde was placed outside of the balloon on the inlet of the, already inflated balloon, as much as possible close to the gravity centre. Hence in the first experiment at INRiM the two models of balloon were tested together. During the experiments the balloons were link to the ground using a small wire, in order to not lose components that could be reused for other experiments.

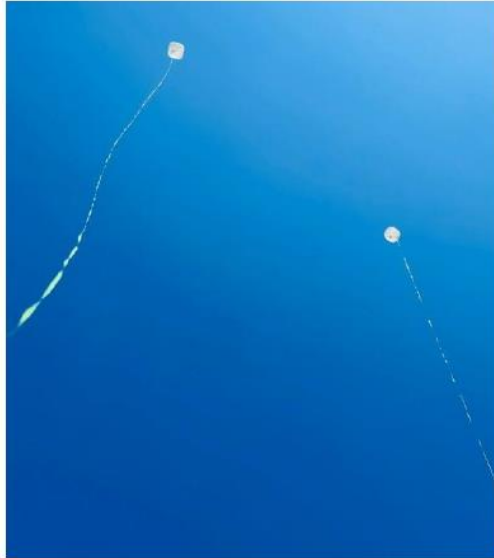


Figure 5.1: Baloons in the first experiment at INRiM

Thanks to this first experiment the model of balloon with the PCB placed outside was chosen as the data measured are more accurate and the position of the PCB does not alter remarkably the system's centre of gravity.

The focus of the second experiment at INRiM was to use five balloons together and receive data from five different mini radioprobes. One of the main difficulties expected from this experiment was related to the transmission system as five PCBs were sending data together and data could overlap. Despite some initial technical problems with the setup of the instrumentation needed, at 14.38 (Rome time) the record of data started and were measured more than one hour data. All the balloons worked well and all the PCBs sent enough data to the computer stations. There were some data missing due to overlap, but enough data were recorded from all the radioprobes in order to get valuable insights. In particular the worst data measured are those of velocity and acceleration. The reason is that both of acceleration and velocity need to be tracked at small intervals of time, using 5 probes has caused higher gaps time between data. Proprieties like temperature, pressure, humidity ad GPS coordinates, that are much more static than acceleration and velocity, are less affected by this transmission problem. When some data are missing and a chronological time history is needed to get insights, I have used the Matlab function Synchronize that interpolates with linear trend the series of data with gaps in the timeline.



Figure 5.2: Baloons in the second experiment at INRiM



Figure 5.3: PCBs in the second experiment at INRiM

After more than one hour of flight the data obtained and filtered are presented in the graphs below.

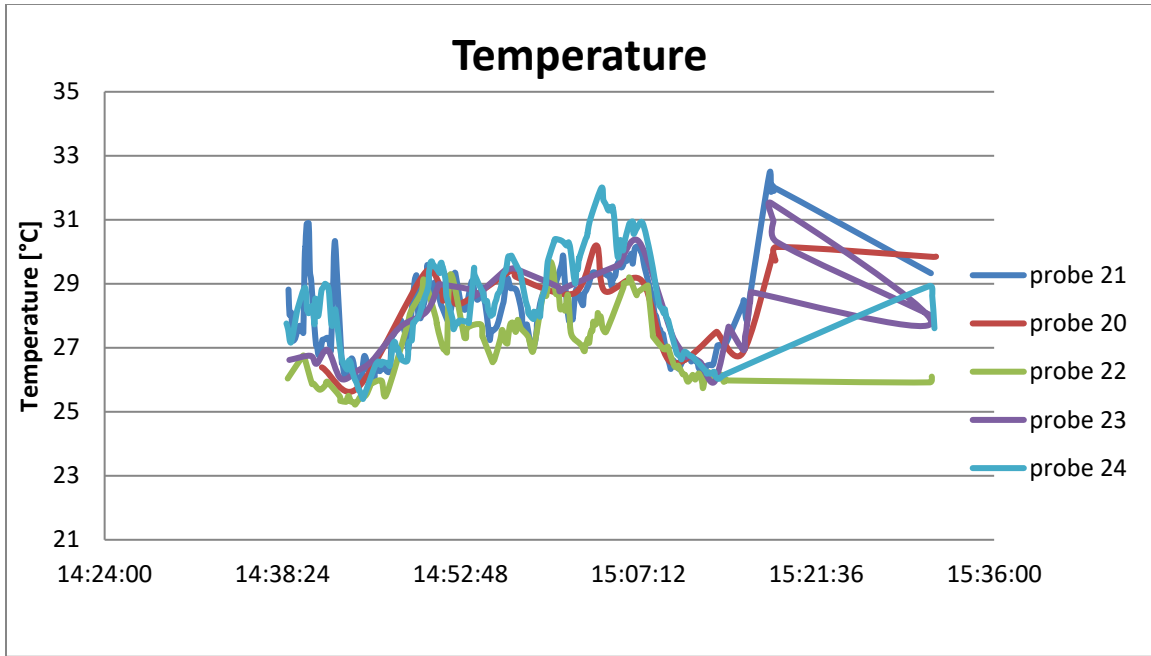


Figure 5.4: Temperature comparison between the five probes

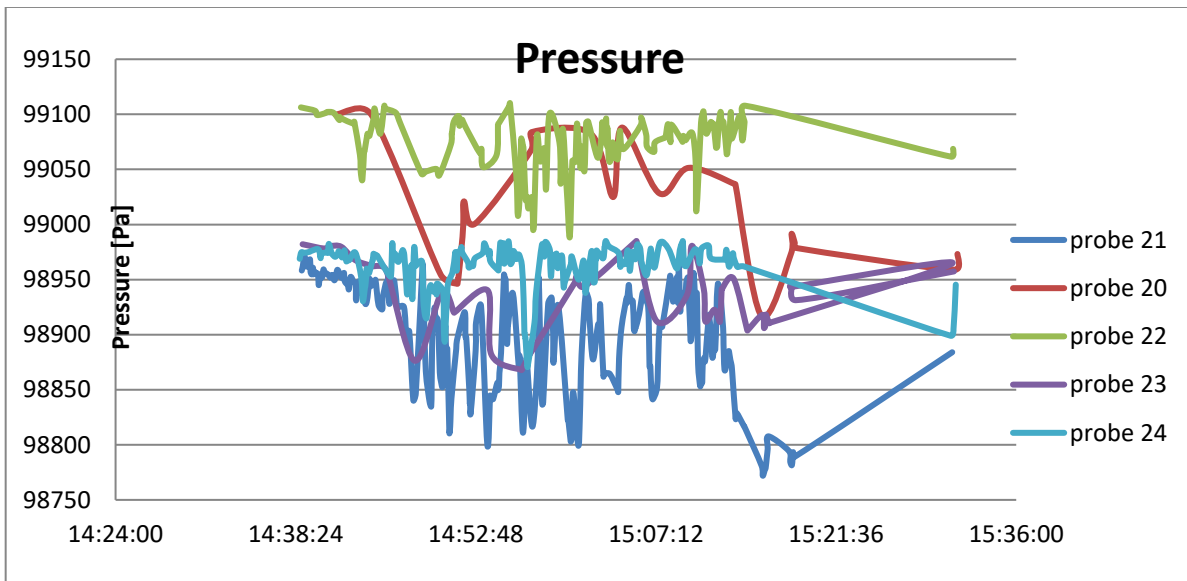


Figure 5.5: Pressure comparison between the five probes

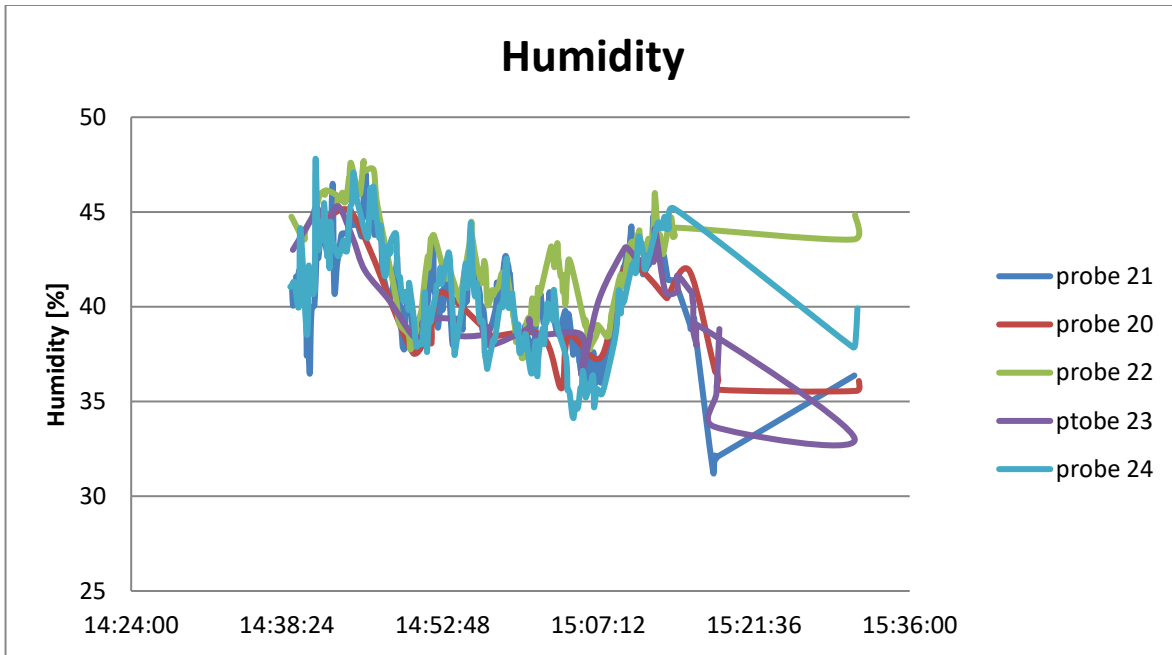


Figure 5.6: Humidity comparison between the five probes

The proper calibration of the probes had been held in the climate chamber (KambicKK190 CHTL) at INRiM. That chamber allows temperature regulation in the range from -40°C to 180°C and relative humidity control in the range 10% to 98% RH. The reference temperature values were obtained through four platinum resistance thermometers (Pt100) calibrated at INRiM laboratory inside the climate chamber; the uncertainty of the Pt100 ranges from 0.011°C for positive temperatures and 0.02°C for negative temperatures. The reference humidity value was obtained with a Delta Ohm humidity and temperature probe calibrated at INRiM connected to a datalogger model HD27.17TS; its uncertainty is $\pm 3\%$. In order to test the sensors and get the possible spread of their behaviour, three radioprobes boards were placed inside the climatic chamber (see table 5.1 to evaluate the mean bias error measured).

In order to evaluate the error between the probes' measurements and the INRiM data, a test of the probes functioning was hold before the proper experiment. The test set up has been placed close to the Vaisala probe, in order to get a comparison as much as possible correct and valuable. The data obtained are presented in the graphs below and the data measured by the five probes are presented as a mean during the time.

Sensors	Mean bias error
---------	-----------------

Accelerometer	0.15 m/s ²
Magnetometer	0.32 gauss
Gyroscope	1.31 dps
Temperature	± 1°C
Pressure	± 100 Pa
Humidity	± 3%

Table 5.1: mean bias error measured in climate chamber

Before the proper start of the experiment hold at INRiM on the 29th of September 2021 in Turin, both the two receivers used were tested close to the Vaisala probe, which is taken as a reference for pressure, temperature and humidity values. The Vaisala probe records daily every minute pressure, temperature and humidity. The data recorded from the tests of the two receivers and those coming out of the Vaisala probe are evaluated below. As long as the received packets are coming from the same sources in both receivers, the following graphs shows only one data set obtained as a combination of the two data set recorded.

In the graphs the 'mean' parameter has been calculated as a mean of the data of each probe. From previous analysis on each data set it has been possible to notice that in the range 11:04 and 11:16 data recorded present some oscillations probably due to sensors adaptation. For that reason, in the following graphs the time on the abscises will start from minute 11:16. It has also been possible to notice for the pressure graphs that probe 20 and 22 show a trend shifted up respect to the other probes. For that reason, the mean and the absolute error of the pressure have been evaluated without probe 20 and 22.

In the following graphs are presented data using only one data set as a combination of the data from the two receivers.

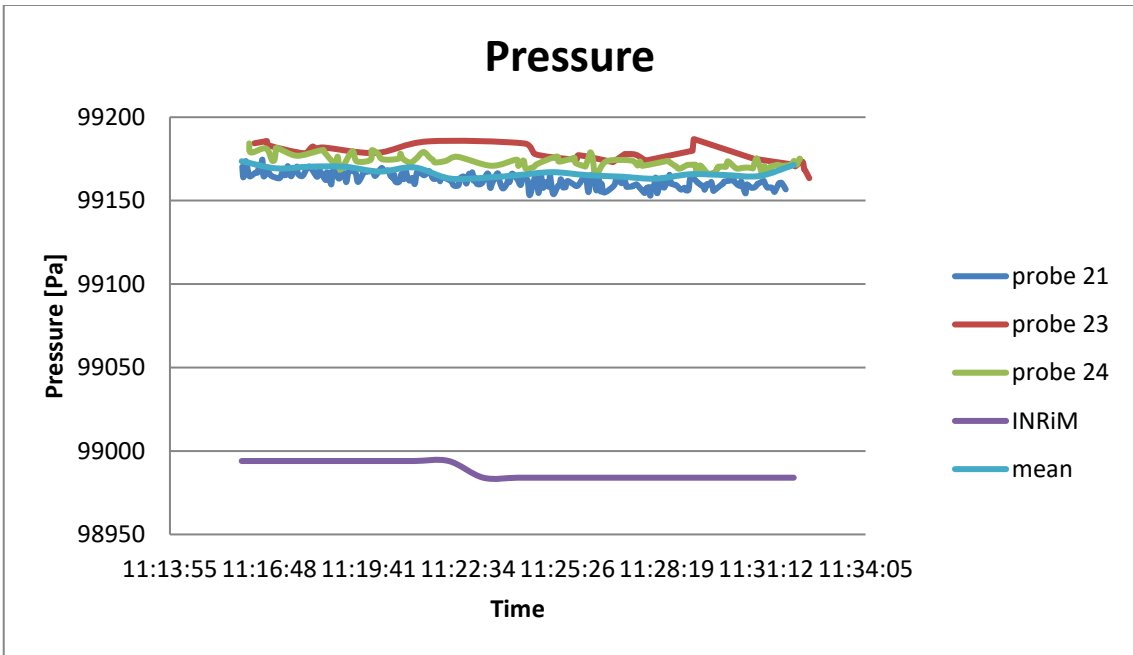


Figure 5.7: Pressure comparison between the probes and Vaisala

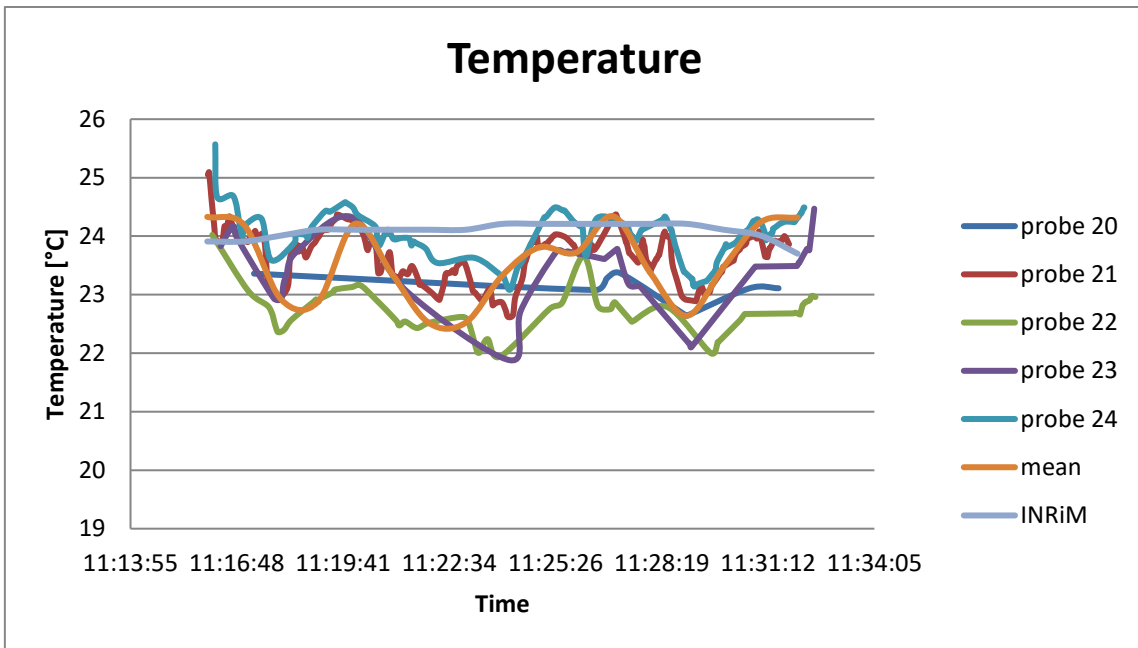


Figure 5.8: Temperature comparison between the probes and Vaisala

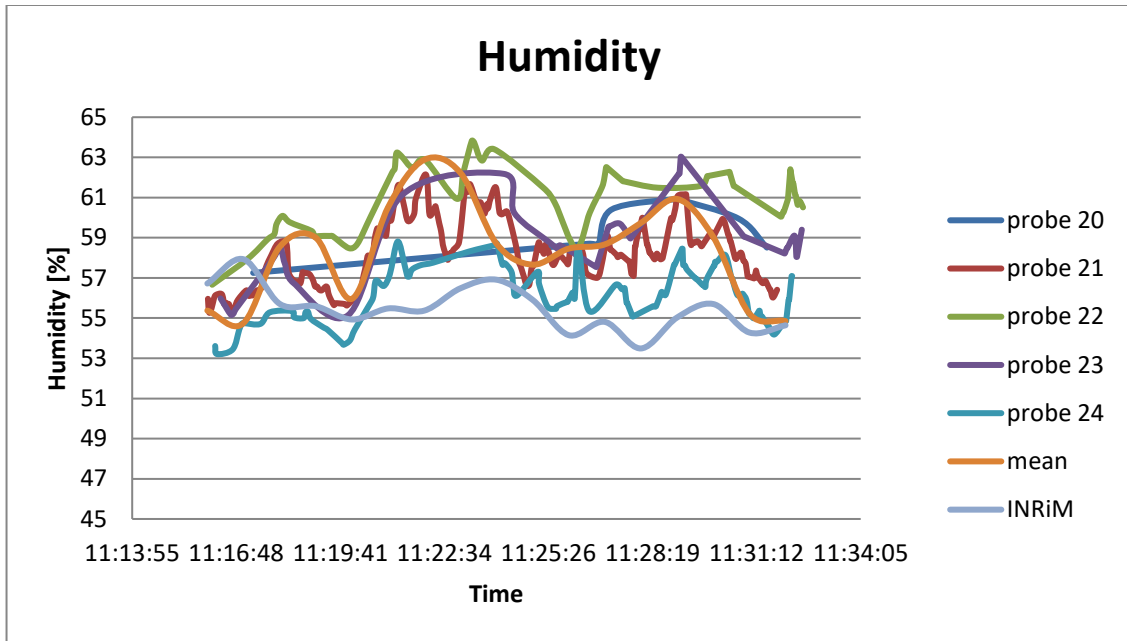


Figure 5.8: Humidity comparison between the probes and Vaisala

Using the mean value, it has been possible to evaluate the error as the module of the difference between the mean and the Vaisala values of pressure, temperature and humidity. Indeed, the Vaisala data are considered the real values. The mean of the errors calculated is then subtracted from the data of each probe. The results are presented in the following graphs.

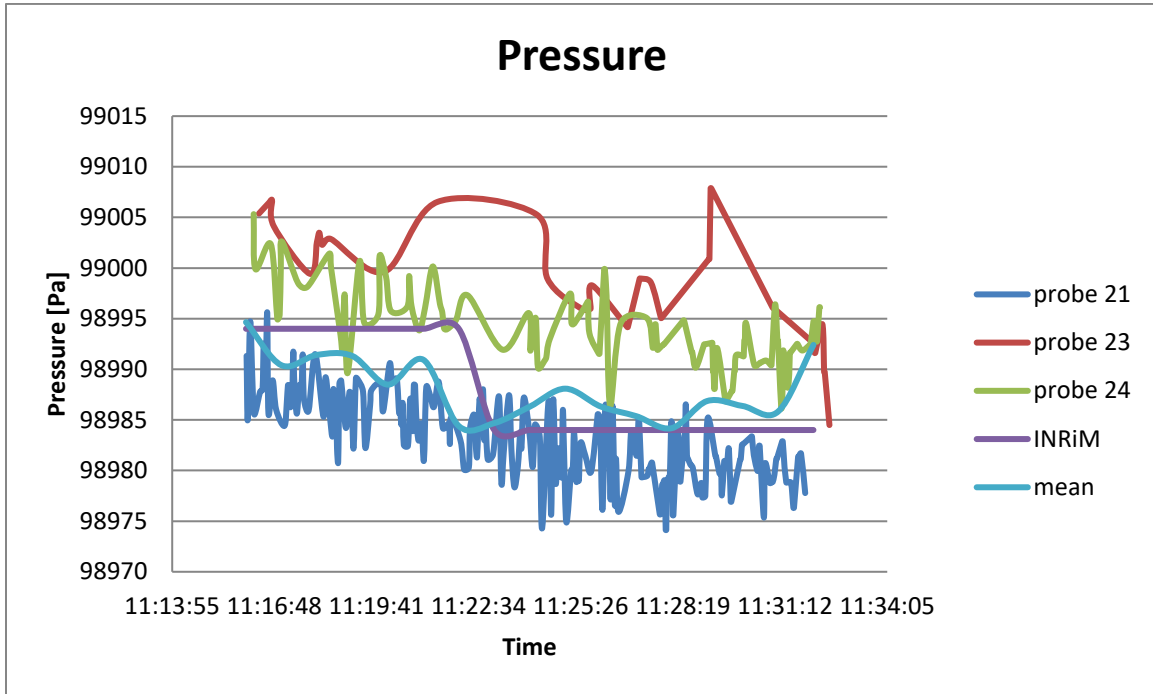


Figure 5.9: Pressure comparison between the probes and Vaisala

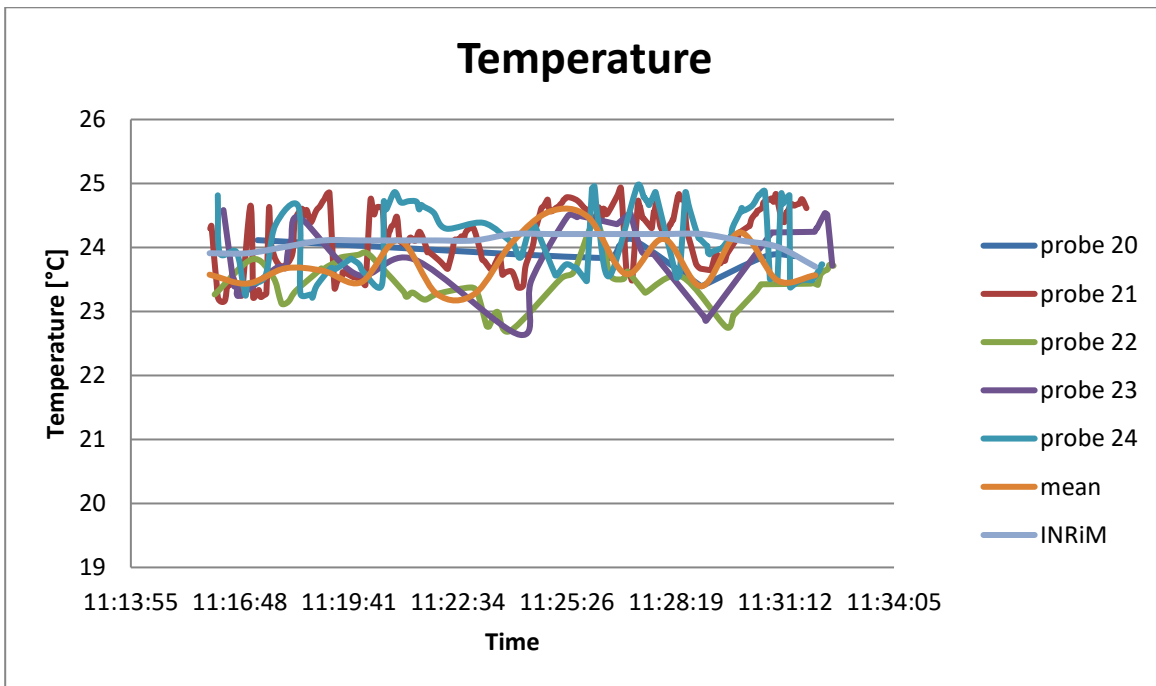


Figure 5.10: Temperature comparison between the probes and Vaisala

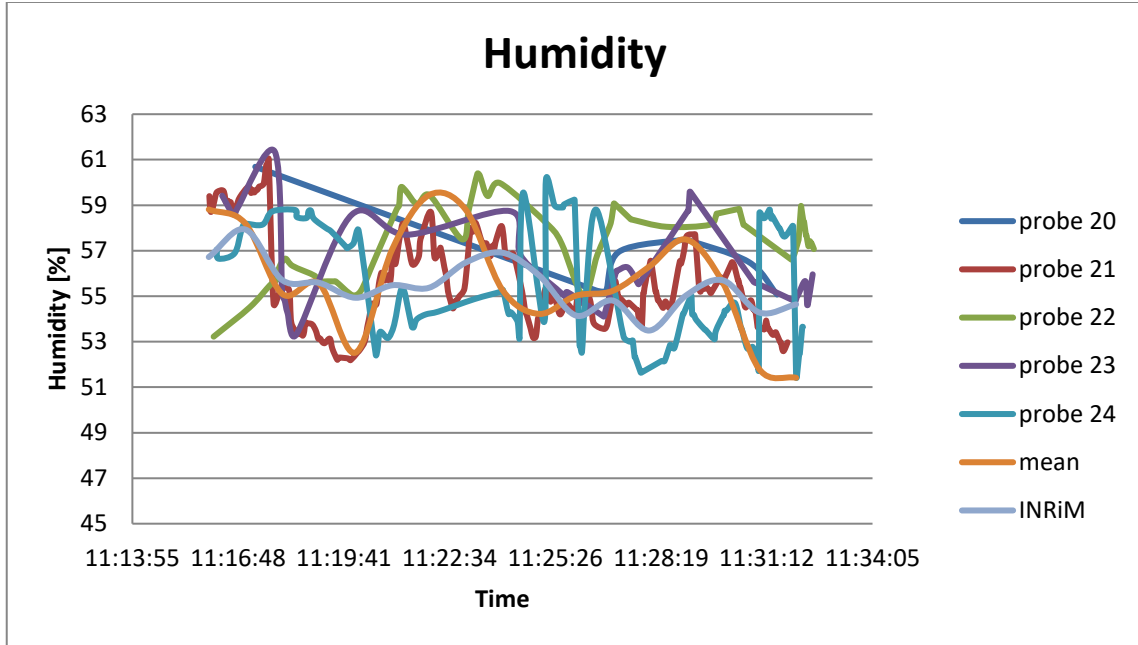


Figure 5.11: Humidity comparison between the probes and Vaisala

The absolute errors evaluated for the test with the receivers are

Absolute error (relative to sensors data)	Values
Δp	179 Pa
ΔT	0.75°C
$\Delta humidity$	3.43 %

BME280 sensor has [61]:

Absolute accuracy (BME specifics)	Values
<i>Absolute accuracy pressure</i>	$\pm 100 Pa$
<i>Absolute accuracy temperature</i>	$\pm 0.5^\circ C$
<i>Absolute accuracy humidity</i>	$\pm 3\%$

In order to obtain a physical measurement of the position of the probes during the first experiment it has been placed a Sony HDV camera. The idea is to validate the GNSs data coming out from the probes using the video recorded during the experiment at INRiM. In particular it has been possible to estimate the distances between the camera and the balloons and, as a consequence, the relative distances between balloons. Evaluating the trend of the distances and comparing the one coming from the GPS data and the

one coming from the video it is possible to validate the GNSS signal. The probes acquire UBX-NAV-PVT packet from GNSS sensor, from which it is possible to extract

- hour, minute and second in UTC0 time zone
- fix (defines the quality of positioning info)
- longitude, latitude and altitude
- velocity in north, east and down directions

It is possible to evaluate the distance of the probes from the camera, which reference position is

- camera longitude 7.639994
- camera latitude 45.016637
- camera altitude 240 m

In figure 5.21 is presented the distance from the camera of the red and black probes in a period of time in which there are enough data the create a comparison between the GPS data sand the record measurements.

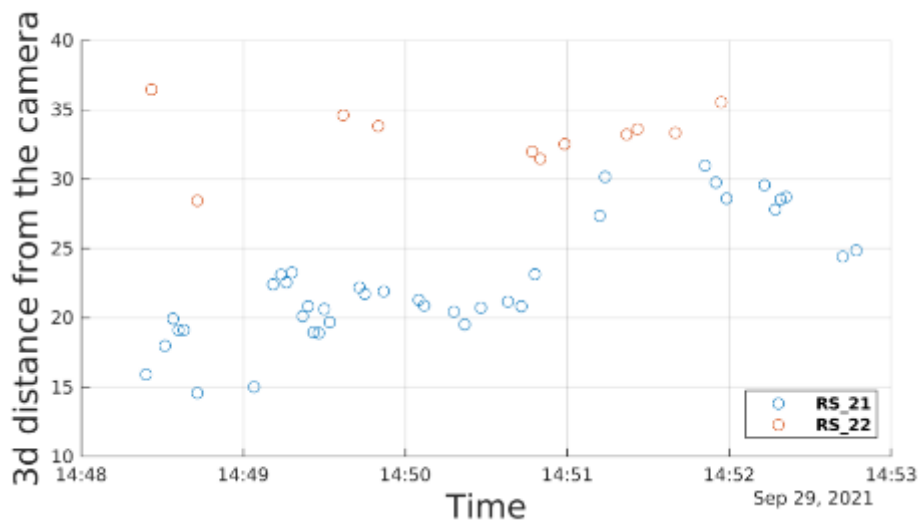


Figure 5.12: Distance computed using data of black and red balloons (RS_21 black balloon, RS_22 red balloon)

Before the start of the experiment at INRiM we have recorded at three different known distances 5 m, 10 m and 25 m a calibrated stick. The idea was to use those records to set a scaling to measure, in the post processing, the distance between the camera and the balloons. Doing the post processing a problem occurred: the zoom and the camera were moved. Indeed, in order to create a correlation between the

physical distance and the dimension of the balloons the zoom and the position of the camera must be fixed. In order to validate data measured by the probes it is necessary just a little time period. It has been selected a time period of 1minute, from 14:49:20 to 14:50:05, as in that slot probes were sending data correctly and both the red and black balloons were visible and were not too far from the camera. For the minute selected in the record every 5 seconds it has been evaluated the dimension of the balloons in the record in terms of pixels. It has been possible to transform these dimensions in the balloon-camera physical distance at every interval of time. Indeed, using the first records, where the calibrated stick was placed at three known different distances, it has been created a linear correlation between the distance of the balloon from the camera and the dimension of the balloon.

This kind of analysis of the records has some limits, the first one is that balloons in the video must be relatively close to the camera and in the line of sight as they are too high, they are seen smaller on the frame, but they are not further from the camera. Another consideration is that the scaling has been assumed linear, in fact should be use as much points as possible to correct the correlation between the dimensions of objects and their distance from the camera.

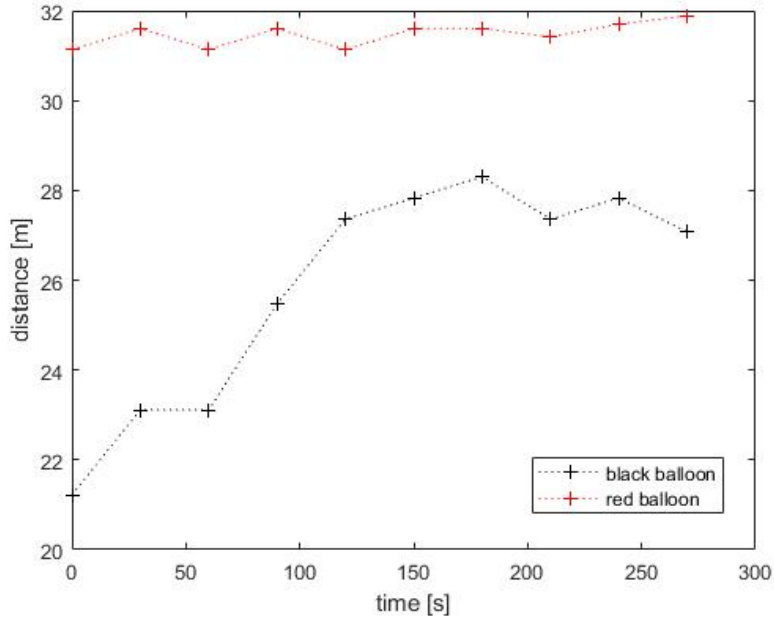


Figure 5.13: Balloon-camera distance measured in the video

This analysis has to be improved for the next experiment, anyway it possible to observe a similar trend between the data coming from the probes and those evaluated in the record. In order to have much more accurate and valuable information from the video it will be used multi-camera set up so that in the post processing will be possible to have a stereo vision analysis of the records. Further details regarding this analysis will be explained in the next paragraph.

It has been possible to evaluate the mean number of neighbors in the simulation domain (Figure 5.15) - as already discussed in chapter 2 - and in the radioprobes' dataset (Figure 5.16).

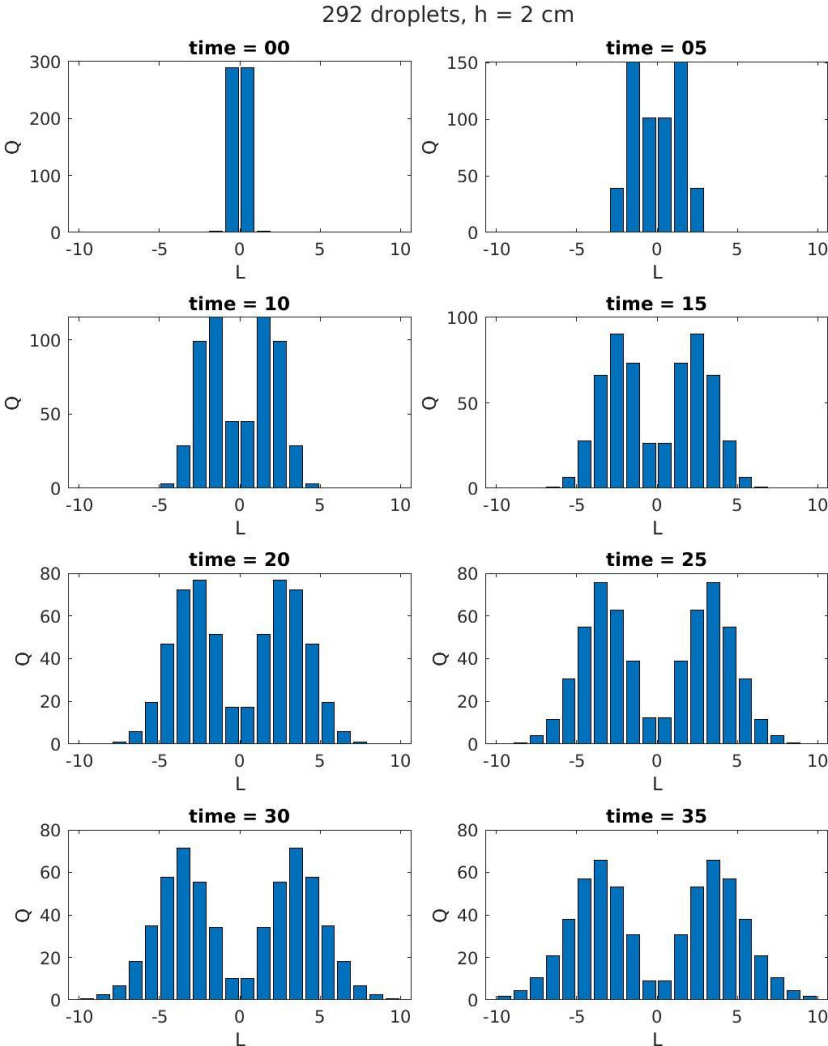


Figure 5.15: $l-Q$ 3D diagram over scalar time. Starting from the initial time where the molecules are all close together and Q has a peak in the first length interval, the molecules spread out and the quantity Q indicates how

many molecules see each other in the specific space range $(n-l, n)h$. When Q has a peak means that there is a cluster of molecules in that $(n-l, n)h$ interval. Respect to figure 2.16, it is possible to notice that Q in the $(0, l)h$ range lowers more quickly over time, that is because the third dimension gives more physical space to the domain considered.

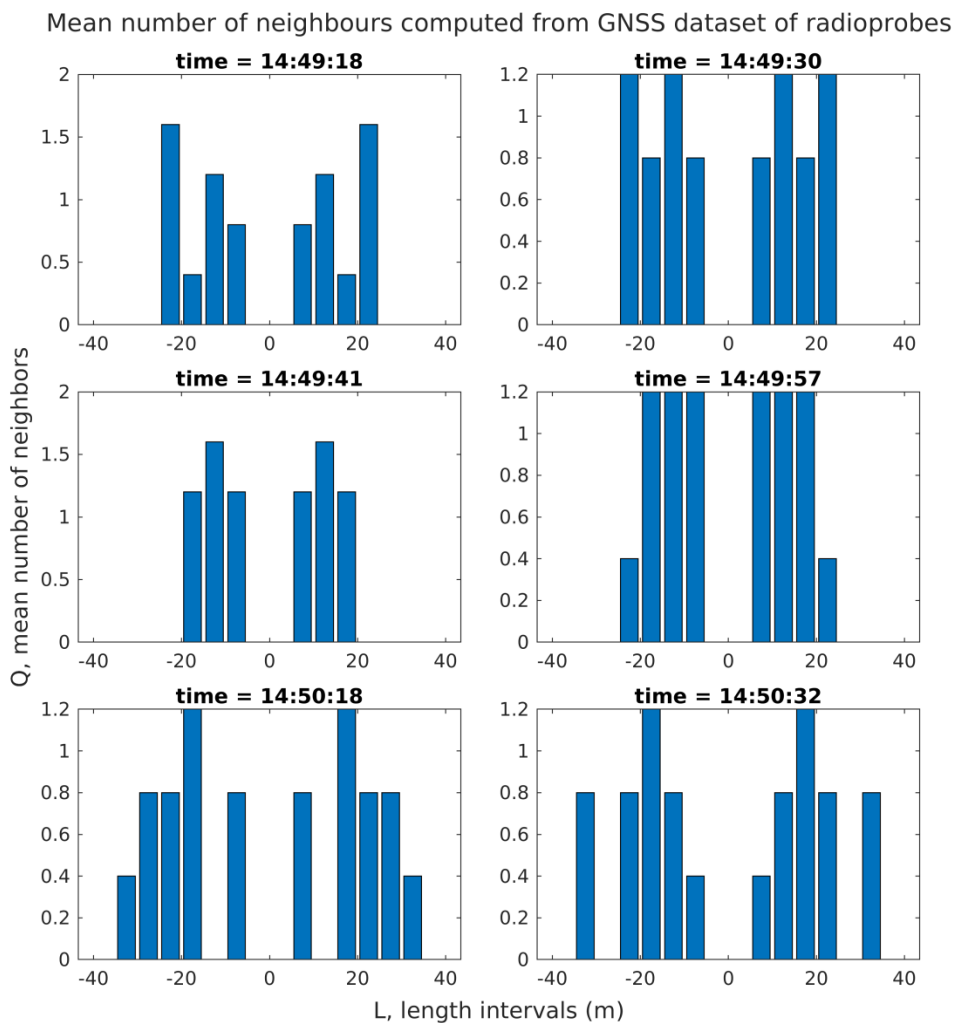


Figure 5.16: $l-Q$ diagram over physical time, the Richardson analysis applied to the probes - for a slot of time when data are considered valuable and there is correspondence to the records - show the expected trend even though the physical phenomenon is not the free dispersion. As long as balloons are linked to the ground there is a bond that does not allow the free dispersion of the probes. Although it is possible to evaluate with the sensors data the relative position of the probes and see, thanks to the quantity Q , where there are clusters in the domain. Another important consideration should be done in respect to the dimensions: the DNS analysis takes place over smaller distances, in the experiments the dimensions of the domain are hundreds of meters

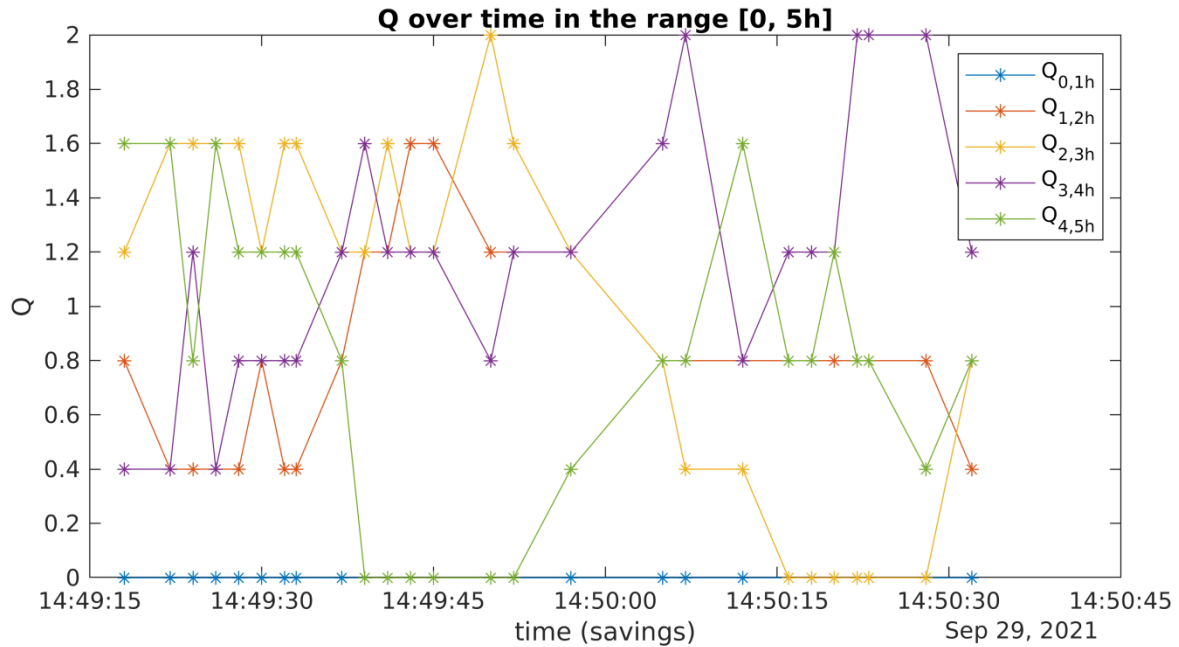


Figure 5.17: Q trend over time for each interval $(n,n+1)h$. This a much more quantitative graphics of the situation presented in figure 5.18, which gives a much more qualitative representation of the phenomenon

5.2 OAVdA experiment

The second experiment was held at the Osservatorio Astronomico della Regione Autonoma Valle d'Aosta (OAVdA) at Lignan, a small village close to Nus. The aim of this second experiment with five radioprobes is to evaluate the behavior of the entire set up in a different and more complex field, as mountains are.



Figure 5.14: OAVdA observatory

During this experiment five radio probes were launched simultaneously, and two cameras were used in order to obtain a more realistic evaluation of the position of the probes. Indeed, using the stereo triangulation, it is possible to obtain spacial information about the recorded items. The setup of the cameras in the field had been defined in order to have a region, recorded by both of the cameras, where all the five balloons could flight without crossing into each other.

In particular both the two cameras had the same set up in terms of resolution and FPS, the distance between the two was chosen at 20m and they were placed on the same line and at the same height. Using technical parameters of the cameras was possible to evaluate the angle of view of the cameras respect to the horizontal and the vertical planes, they are respectively 60° and 45° . In particular using 20 m as a distance between the two cameras and 45° as inclination of the focal axes respect to the horizontal line it has been possible to a have an ideal sketch of the record's field. Using basic trigonometry, it has been possible to evaluate some points on the external perimeter of the field recorded by both of the cameras that is the area in which the balloon should float. Using the value of the vertical angle of view of the camera and its height from the ground it has been possible to determine the length of the thread of the balloons, which was around 15m. During the entire experiment focus and zoon were fixed. In that thesis

the data from the cameras will not be evaluated due to the lack of time, anyway the idea for future analysis is to compute the stereo vision evaluation using already existing tools.

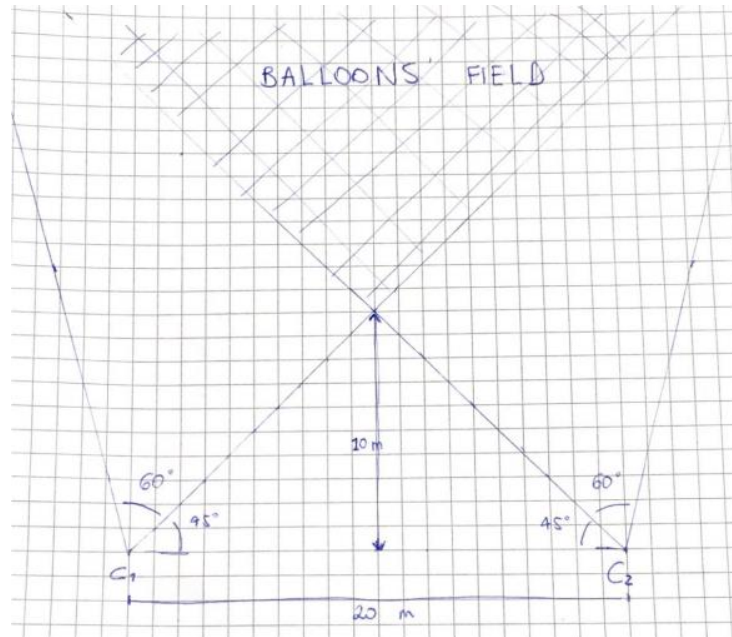


Figure 5.15: Balloons' field set up; the field in which the balloons fly is recorded simultaneously by both of the cameras in order to do a stereo vision analysis.



Figure 5.16: Balloons' field, we also had the possibility to use the electrical sticks as a support for the balloons

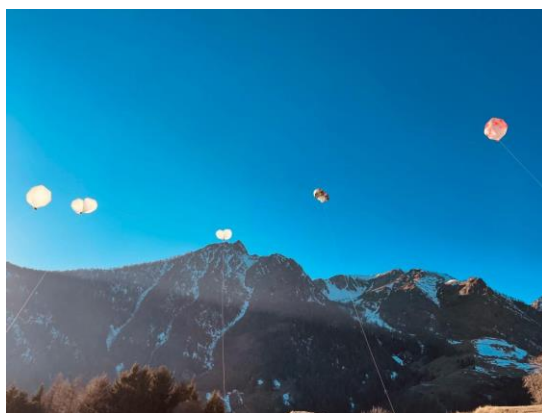


Figure 5.15: Balloons flying test

From the previous experiment it has been possible to observe that the heat produced by the battery could affect the data measured by the sensors. Therefore, in this experiment the battery was isolated from the PCBs by a little layer of sponge. That small layer was light enough not to require an additional balloon's lift. The wire used was a cylindrical one in order to minimize the 'sail' effect of the 'presents' thread used in the previous experiment.



Figure 5.16: PCB's new set up with isolation sponge

In the following graphs are presented data obtained from the experiment. The first three graphs show the trend of pressure, temperature and humidity measured by the five probes all together. As in the previous experiment probes 20 and 22 show a relevant difference in the pressure measurements from the other probes, for that reason they have not been take in consideration in the mean and for the evaluation of the absolute error. Respect to the other experiment the data oscillate more, that could be related to the different kind of external condition in which the probes have been tested.

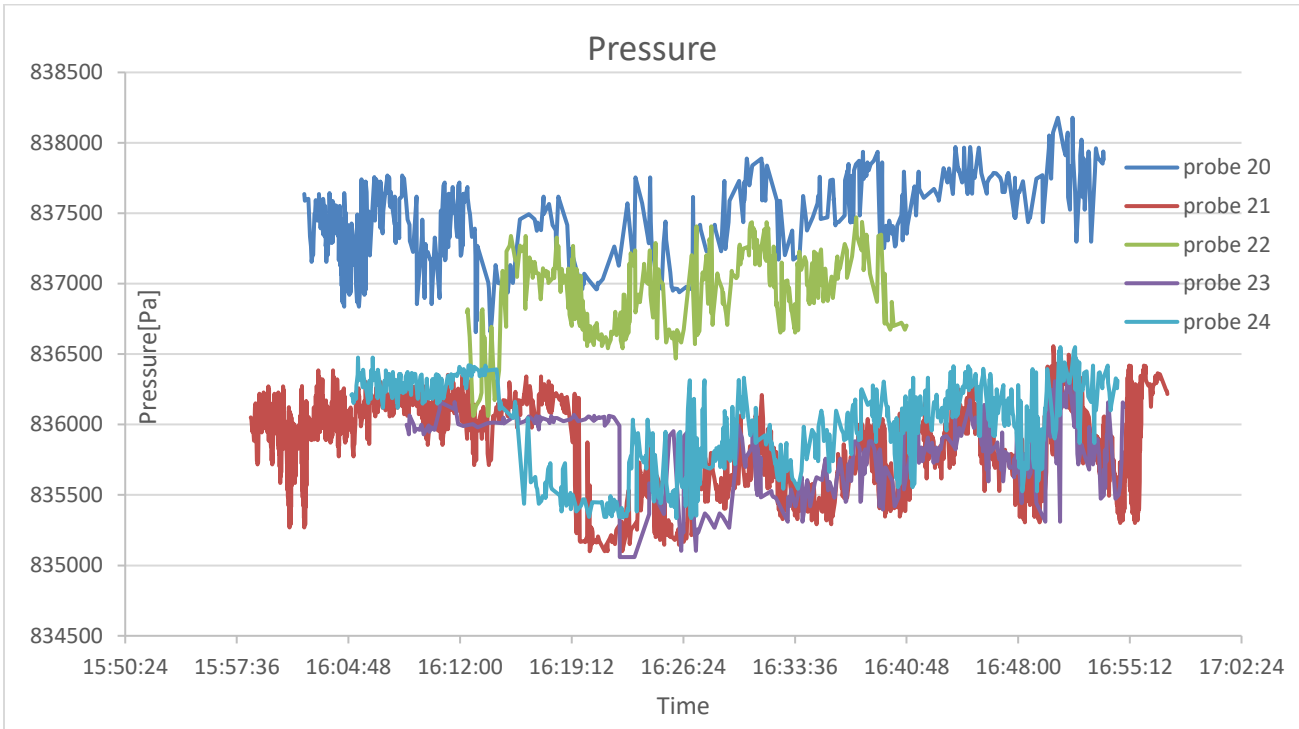


Figure 5.17: Pressure comparison between the five probes

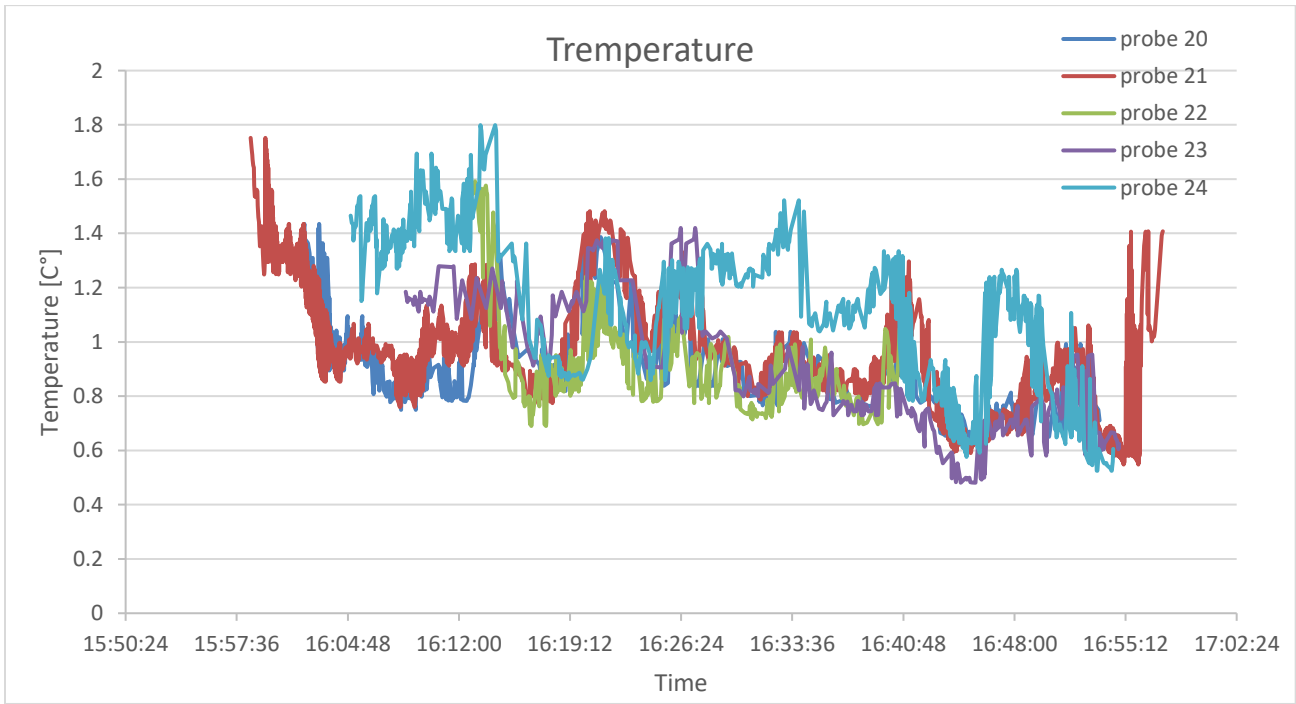


Figure 5.18: Temperature comparison between the five probes

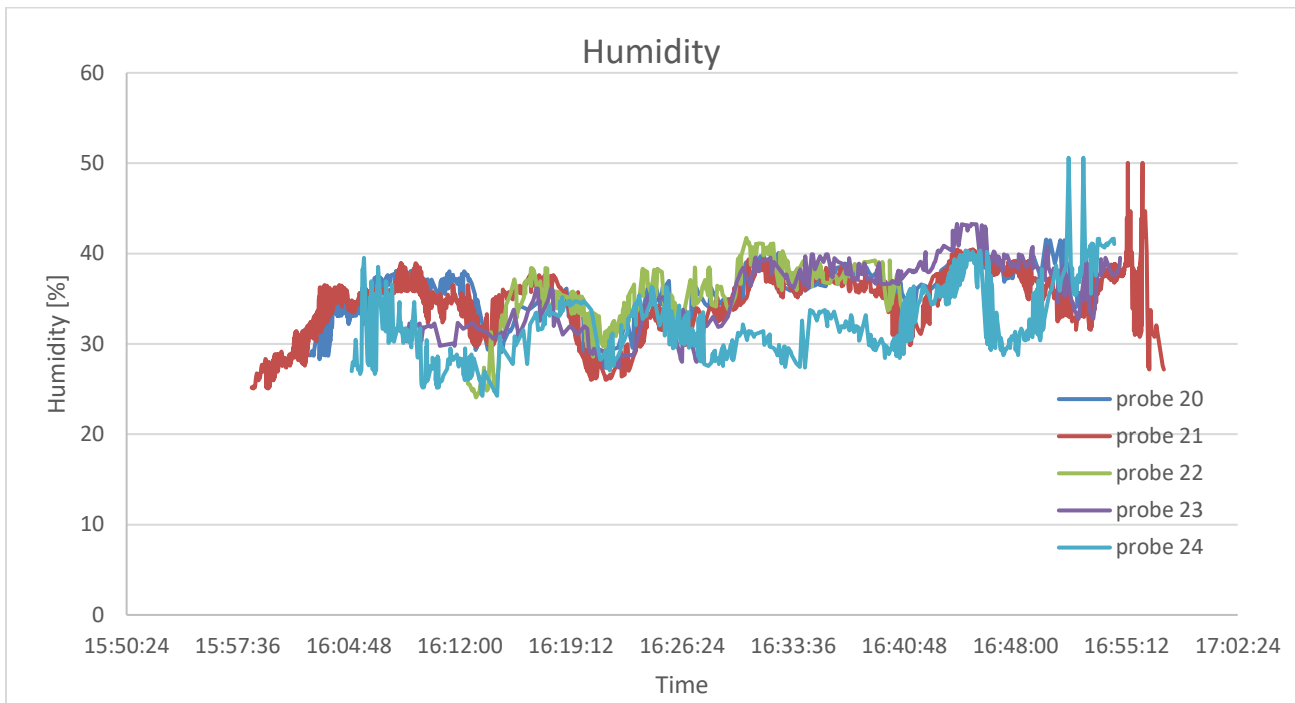


Figure 5.19: Humidity comparison between the five probes

Before the proper start of the experiment hold at OAVdA, both the two receivers used were tested close to the Saint-Barthelemy station (more information about the net of Functional Centre and Arpa stations are available at https://presidi2.regione.vda.it/str_dataview), those tests are useful to better analyze the error relater to probes' measurements. The data measured by the station are taken as a reference for pressure, temperature and humidity. The station records daily every ten minutes many parameters; the following analysis considers pressure [hPa], temperature [°C] and humidity [%]. The data recorded from the tests of the two receivers and those coming out of the station are evaluated below. As the received packets of data are coming from the same sources in both receivers, the following graphs shows only one data set obtained as a combination of the two data set recorded.

As already explained in the previous subchapter, the 'mean' parameter has been calculated as a mean of the data of each probe. It has been possible to notice that data recorded present many oscillations about the mean value, probably due to sensors adaptation and the alpine environment. It has also been possible to notice for the pressure graphs that probe 20 and 22 show a trend shifted up respect to the other probes.

For that reason, the mean and the absolute error of the pressure have been evaluated without probe 20 and 22.

In the following graphs are presented data using only one data set as a combination of the data from the two receivers. The fact that the data measured shows much more fluctuations is also due to the fact that the data from the OAVdA station are mediated in range of ten minutes. Using the mean value, it has been possible to evaluate the error as the module of the difference between the mean and the OAVdA station values of pressure, temperature and humidity. Indeed, for that analysis the OAVdA data are considered real values. The mean of the errors calculated is then subtracted from the data of each probe. The results are presented in the following graphs and are summarized in the table that follows them.

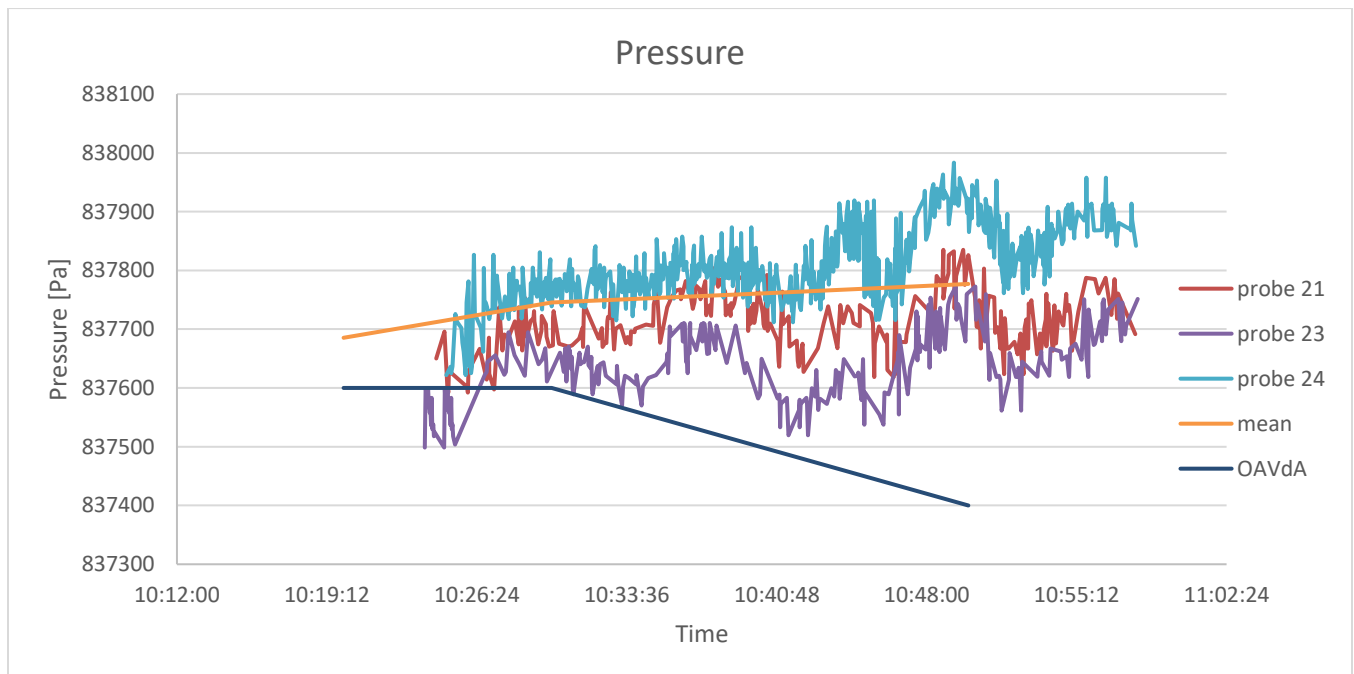


Figure 5.20: Pressure comparison between the probes and the station

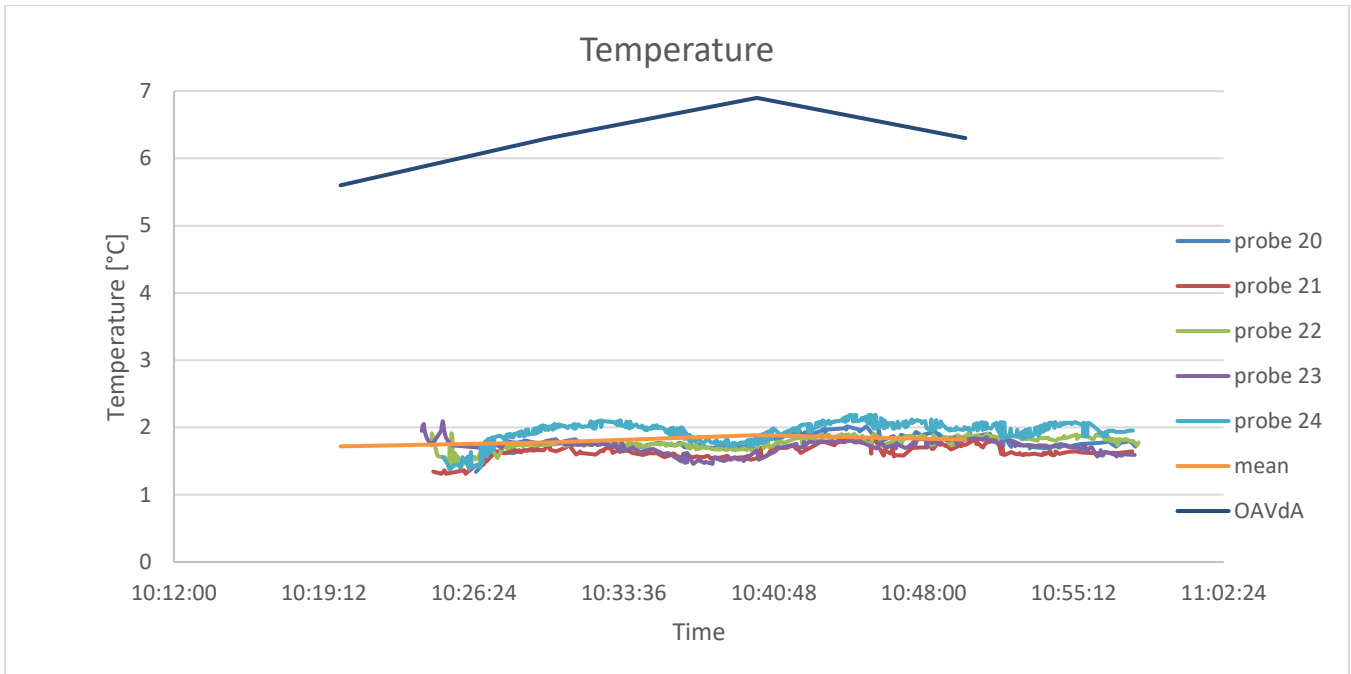


Figure 5.21: Temperature comparison between the probes and the station

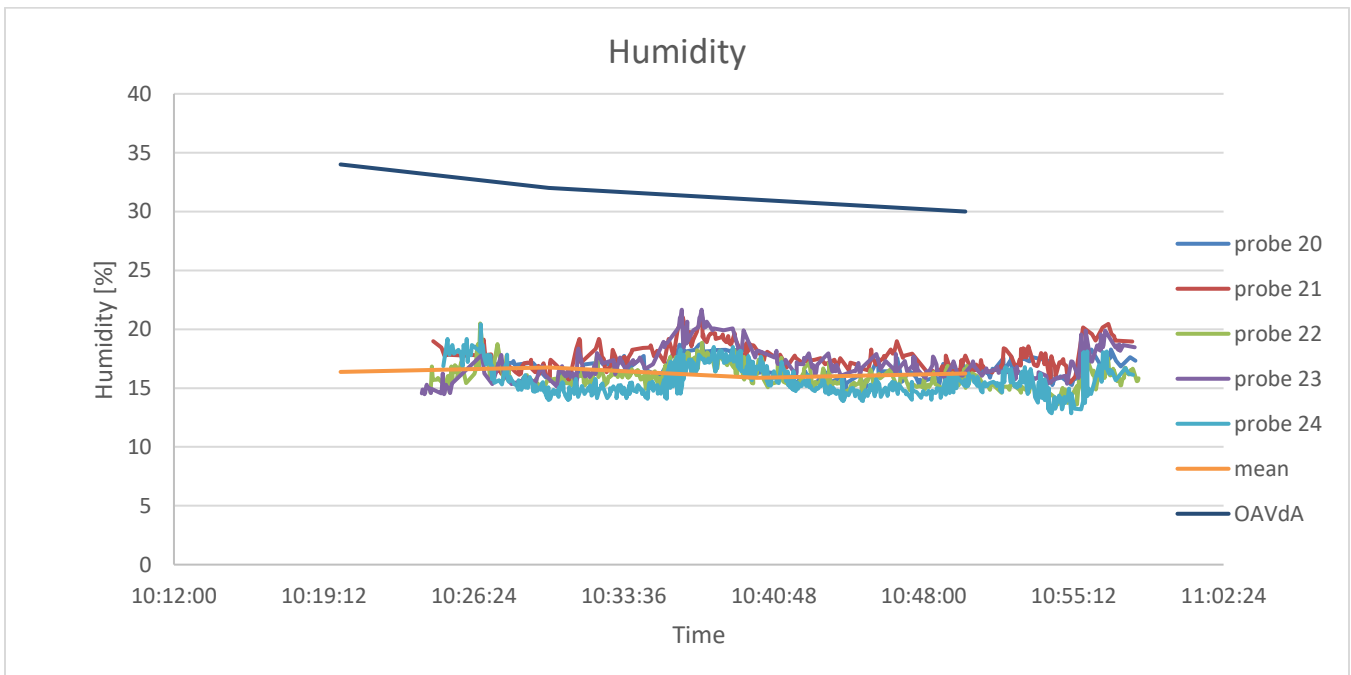


Figure 5.22: Humidity comparison between the probes and the station

Using the mean value, it has been possible to evaluate the error as the absolute value of the difference between the mean and the station values of pressure, temperature and humidity. Indeed, the station data are considered the real values. The mean of the errors calculated is then subtracted from the data of each probe. The results are presented in the following graphs.

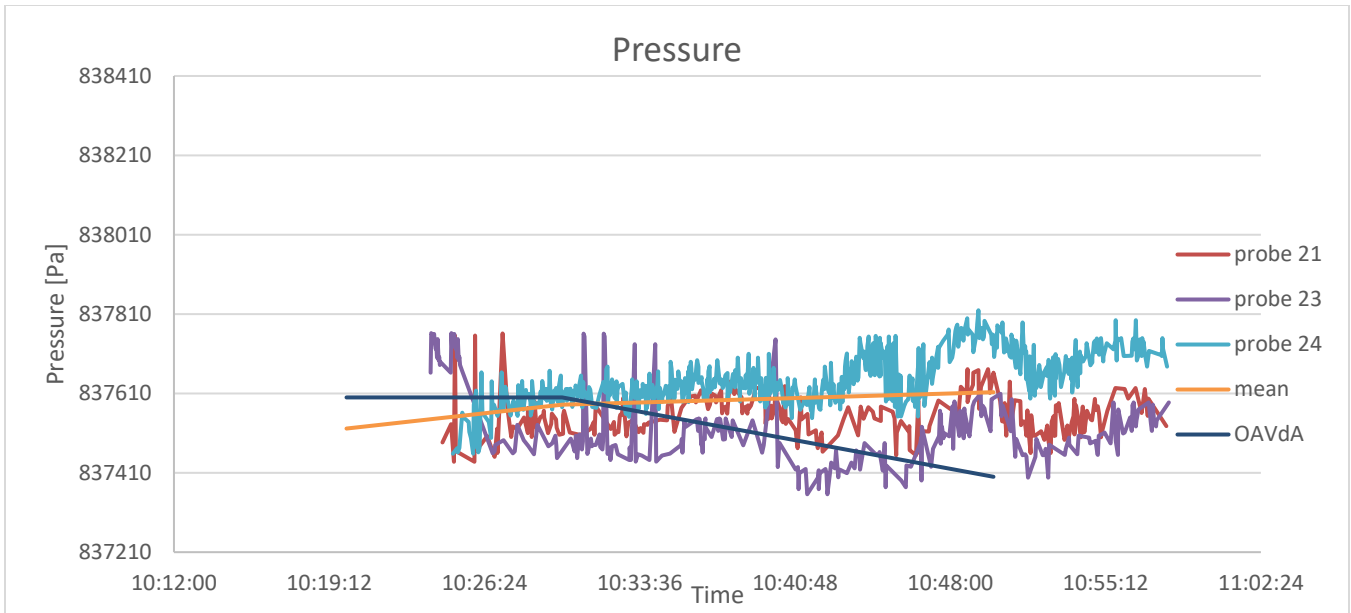


Figure 5.23: Pressure comparison between the probes and the station

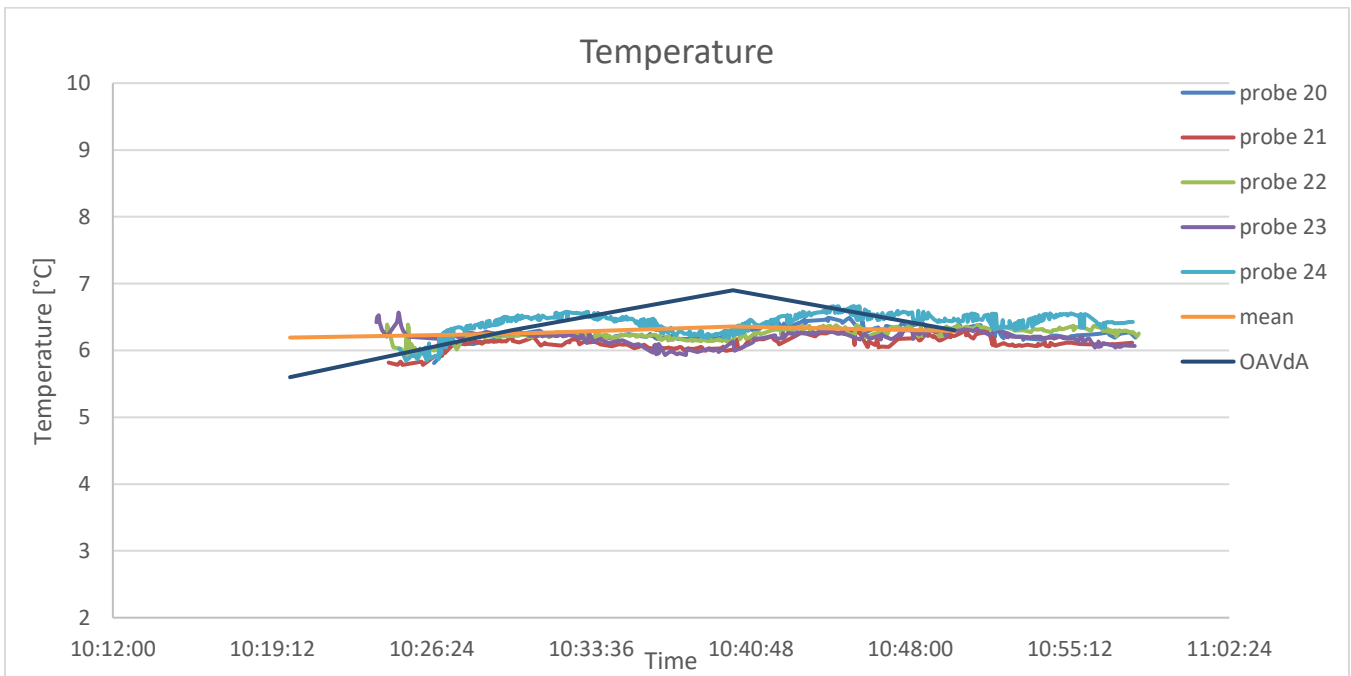


Figure 5.24: Temperature comparison between the probes and the station

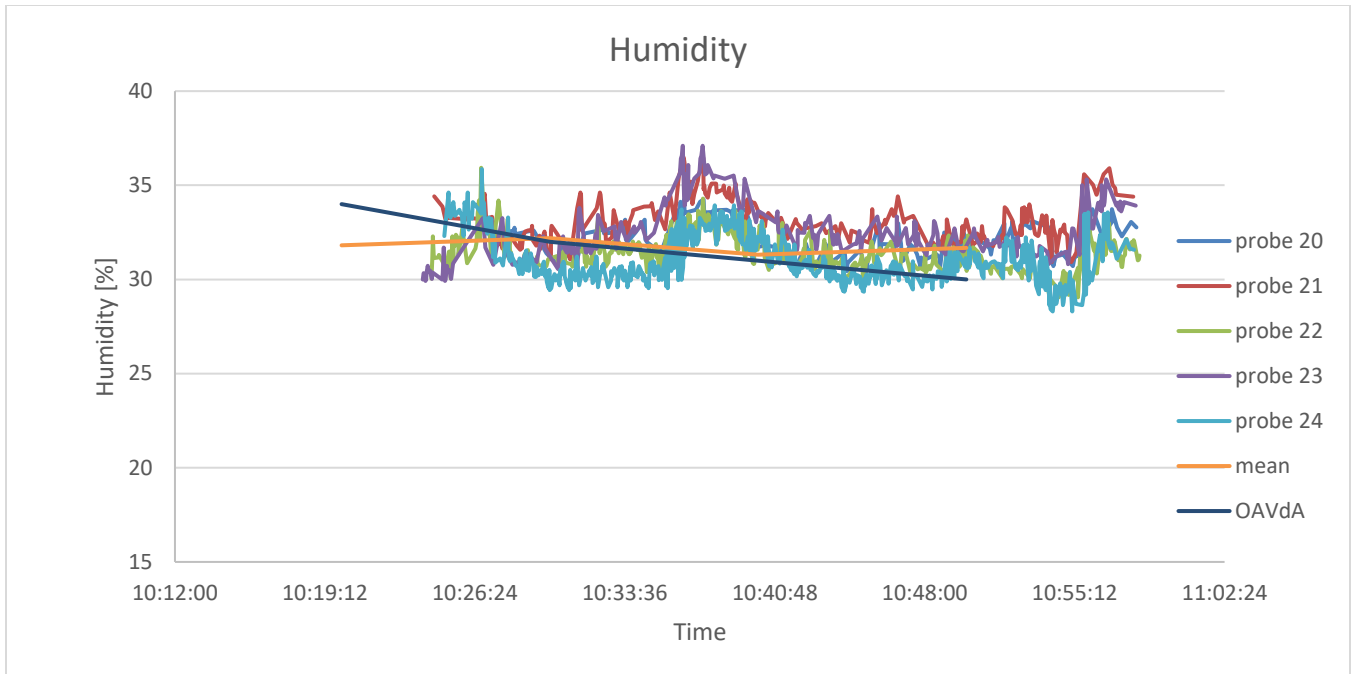


Figure 5.25: Humidity comparison between the probes and the station

The absolute errors evaluated for the test with the receives are

Absolute error (relative to sensors data)	Values
Δp	163 Pa
ΔT	4.47°C
$\Delta humidity$	15.4 %

BME280 sensor has [61]:

Absolute accuracy (sensors specifics)	Values
<i>Absolute accuracy pressure</i>	$\pm 100 Pa$
<i>Absolute accuracy temperature</i>	$\pm 0.5^{\circ}C$
<i>Absolute accuracy humidity</i>	$\pm 3\%$

Chapter 6

Conclusion and further developments

The aim of the first chapters of his work is to point out the actual level of knowledge about clouds: their formation, growth and evolution following droplets. Turbulent phenomena inside clouds considerably complicate the system but, at the same time, they determine most of the phases of the development of droplets and general behavior of clouds.

The lack of knowledge is partly due to the difficulty in understanding the physics behind the complex phenomena inside clouds and partly due to the scarcity of in situ measurements. Following the droplets inside clouds from a Lagrangian point of view could give a better understanding of the motions and trajectory inside clouds.

The Horizon2020 Innovative Training Network Cloud-MicroPhysicsTurbulence-Telemetry (MSCA-ITN-COMPLETE) project, illustrated in this work, has the aim to develop small radio-probes capable of following the motion of clouds, floating inside them, and transmitting Lagrangian-type information in real time. The operating principles, the electronics of the system and the choice of materials has been explained in this thesis. Many analyses were made to estimate the right dimensions of the balloons and the correct suspension of the probe in mid-air. Every single component of the PCB was essential to determine the needed hydrostatic thrust and therefore the balloons dimensions; many tests were carried out in the Laboratory to design and develop the best shape of the balloon without complicating too much the structure given the fragility of the Mater-Bi.

Tests and experiments, regarding the behavior of the probes, have been carried out before my proper activity inside the project team. In particular the aim of the first experiment I was involved in, was to test as many radio probes as possible together. The idea of this experiment was to evaluate and obtain a qualitative conception about the dispersion of the probes due to turbulence diffusion. That has been achieved in two different ways: using the GNSS data from the probes and a professional video camera.

Using the 3-D coordinates of the probes it has been possible to determine numerically the relative position of the probes. That analysis has been validated using the relative position of the probes computed from the video.

That experiment has been challenging from different aspects but has been fundamental to organize the following experiment at OAVdA observatory. In particular, at INRiM we have had many difficulties using the professional camera. Indeed, organizing the following experiment in OAVdA, we have decided to use two different professional cameras, in order to do a proper stereo vision analysis, and we have also decided in advance the set-up of the cameras in terms of focus, zoom, focal angles and distances. Another improvement we have done was related to the thread of the balloons: we have noticed that the 'present-like' thread, used at INRiM, tended to pull down balloons, therefore we used a much more cylindric and thin tread. We have noticed, from the data of the first experiment, that the temperature of the battery influenced the sensors records, therefore we have decided to isolate the battery from the electrical circuit with a sponge thin layer. We have also noticed that the balloon in both experiments did not work properly, therefore one of the future improvements we are working on is to develop, in collaboration with the Italian Institute of Technology (IIT), a much more standardized way to obtain the balloons shape instead of building it manually every time.

Ringraziamenti

Un ringraziamento speciale alla professoressa Daniela Tordella che mi ha seguito in questi sei mesi e che mi ha dato l'opportunità di prendere parte a questo progetto internazionale. Mi ha dato la possibilità di conoscere realtà di eccellenza sul territorio italiano come l'istituto INRiM e l'osservatorio OAVdA, di lavorare con un gruppo di ragazzi provenienti da tutto il mondo e infine di approfondire in modo interdisciplinare tematiche inerenti non soltanto al mio percorso di studi ma anche molto attuali.

Ringrazio il dottor Shahbozbek Abdunabiev che è sempre stato disponibile per un consiglio e un aiuto in questi mesi, Mina Golshan che si è sempre messa a disposizione per aiutare e organizzare le attività sperimentali e Andrea Caporali che mi ha introdotto e inserito nell'attività fin dal primo giorno.

Ringrazio la mia famiglia per avermi sostenuto, non soltanto in quest'ultimo periodo, ma fin dall'inizio di questo percorso. Grazie mamma per avermi sempre spronata a non mollare e avermi sempre ricordato l'obiettivo finale, grazie Franci e Albi per essere stati sempre al mio fianco e infine grazie Kilian, il fratello peloso migliore che ci sia, che ormai da tre anni e mezzo sei diventato parte integrante e fondamentale della famiglia. Un grazie speciale a papà che mi ha trasmesso la passione per lo sport, grazie per tutte le corse e pedalate insieme che porterò sempre nel cuore. Un pensiero speciale, che vale molto di più di un grazie, lo mando ai miei nonni.

Un ringraziamento speciale a Chiara che ormai da più di dieci anni è molto di più di una semplice amica, una persona grazie e con la quale sono cresciuta tantissimo e ho capito il vero valore dell'amicizia. Dovunque saremo e qualsiasi cosa faremo nei prossimi anni, so per certo che ci saremo l'una per l'altra.

Un grazie speciale a Ludovica M. per tutti i consigli che mi dato in questi anni e per avermi sempre lasciato una fetta di crostata alle nocciole; un altro grazie speciale va a Ludovica R. con cui ho condiviso i più bei viaggi fatti fin'ora e un sacco di risate.

Un grazie speciale a Marti, Fra, Fabio che fin dalle elementari sono stati al mio fianco e un grazie speciale anche ad Alex, Pier, Vitto, Michele e tutti a gli altri compagni conosciuti al Poli con cui ho condiviso alti e bassi di questi ultimi cinque anni.

Infine ringrazio tutte le ragazze e i ragazzi con cui ho condiviso e condivido ancora corse, pedalate e sciate, che mi hanno sempre motivata e sostenuta nello sport, la mia più grande passione.

Whole bibliography

- [1] Tessa C. Bassol , G. Perotto, A. Athanassio, M. Paredes, F. Canavero, A. Merlone, C. Musacchio & D. Tordella, "Development and testing of innovative, mini, biodegradable radiosondes to track small-scale fluctuations in warm cloud and clear air environments".
- [2] B. J. Devenish et al. (2012). Droplet Growth in warm turbulent clouds. Q. J. Roy. Meteor. Soc. 138(667), pp. 1401-1429
- [3] COMPLETE ITN - ETN NETWORK Horizon 2020. (2017). Available from: <https://www.complete-h2020network.eu/>
- [4] S. Businger, et al., "Scientific insights from four generations of Lagrangian smart balloons in atmospheric research". Bulletin of the American Meteorological Society, 87(11), pp.1539-1554 2006.
- [5] S. P. Malinowski et al "Physics of Stratocumulus Top (POST): turbulent mixing across the capping inversion", Atmos. Chem. Phys., 13, 12171-12186 2013.
- [6] J. Heintzenberg, R.J. Charlson, "Clouds in the Perturbed Climate System: Their Relationship to Energy Balance, Atmospheric Dynamics, and Precipitation" Strüngmann Forum Reports. (Eds.) MIT Press: Cambridge, MA, USA, 2009; ISBN 978-0-262-01287-4
- [7] H. Siebert; H. Franke; K. Lehmann; R. Maser; E.W. Saw; D. Schell; R.A. Shaw; M. Wendisch, "Probing Finescale Dynamics and Microphysics of Clouds with Helicopter-Borne Measurements". Bull. Am. Meteorol. Soc. 2006, 87, 1727–1738
- [8] Physics and Chemistry of Clouds Dennis Lamb and Johannes Verlinde
- [9] [Online] Available: <http://www.meteoronciglione.net/?q=le-nubi-nomenclatura-e-loro-classificazione>
- [10] [Online] Available: <https://www.inmeteo.net/2012/06/28/i-cirri/>
- [11] [Online] Available: <https://passioneperlameteo.wordpress.com/atlante-delle-nuvole/>
- [12] [Online] Available: <http://www.fenomenitemporaleschi.it/cumuliforme.htm>
- [13] W. M. Organization. (). International Cloud Atlas, [Online]. Available: <https://cloudatlas.wmo.int/en/clouds-definitions.html>
- [14] H. Pruppacher and J. Klett, "Microphysics of Clouds and Precipitation". Springer Science+Business Media B.V., 2010, ISBN: 978-0-7923-4211-3

- [15] Beard and Ochs, “Warm Rain Initiation: An Overview of Microphysical Mechanisms”, *Journal of Applied Meteorology*, vol. 32, pp. 608–625, 1993.
- [16] W. Grabowski and L. Wang, “Growth of cloud droplets in a turbulent environment”, *Annual Reviews*, vol. 45, pp. 293–324, 2013.
- [17] V. Khvorostyanov and J. Curry, “Toward the theory of stochastic condensation in clouds. Part I: A general kinetic equation”, *J. Atmos. Sci.*, vol. 56, pp. 3985–3996, 1999.
- [18] B. Devenish, P. Bartello, J. Brenguier, L. Collins, W. Grabowski, R. IJzermans, S. Malinowski, M. Reeks, J. Vassilicos, L. Wang, and Z. Warhaft, “Droplet growth in warm turbulent clouds”, *Q. J. R. Meteorol. Soc.*, vol. 138, pp. 1401–1429, 2012.
- [19] M. Pinsky and A. Khain, “Fine structure of cloud droplet concentration as seen from the Fast-FSSP measurements. Part I: Method of analysis and preliminary results”, *J. Appl. Met.*, vol. 40, pp. 1515–1537.
- [20] “Atmospheric Physics” - Adrian Tompkins, ICTP.
- [21] J. Warner, “The Microstructure of Cumulus Cloud. Part I. General Features of the Droplet Spectrum”, *J. Atmos. Sci.*, vol. 26, pp. 1049–1059, 1969.
- [22] P. Jonas, “Turbulence and cloud Microphysics”, *Atmospheric Research*, vol. 40, pp. 283–306, 1996.
- [23] J. Brenguier, “Observations of cloud microstructure at the centimeter scale”, *J. Appl. Meteorol.*, vol. 32, pp. 783–793, 1993.
- [24] H. Siebert, S. Gerashenko, A. Gylfason, K. Lehmann, L. R. Collins, R. A. Shaw, and Z. Warhaft, “Towards understanding the role of turbulence on droplets in clouds: In situ laboratory measurements”, *Atmospheric Research*, vol. 97, pp. 426–437, 2010.
- [25] W. Grabowski and L. P. Wang, “Growth of Cloud Droplets in a Turbulent Environment” *Annu. Rev. Fluid Mech.* 2013. 45:293–324.
- [26] H. Siebert, K. Lehmann, and M. Wendisch, “Observations of Small-Scale Turbulence and Energy Dissipation Rates in the Cloudy Boundary Layer”, *J. Atmos. Sci.*, vol. 63, pp. 1451–1466, 2006.
- [27] J. I. MacPherson and G. A. Isaac, “Turbulent characteristics of some Canadian cumulus clouds”. *Journal of Applied Meteorology and Climatology* 16, 81–90, 1977.
- [28] H. E. Gerber, G. M. Frick, J. B. Jensen and J. G. Hudson, “Entrainment, mixing, and microphysics in trade-wind cumulus”. *Journal of the Meteorological Society of Japan* 86A, 87–106, 2008.
- [29] Y. Xue, L. Wang, and W. Grabowski, “Growth of cloud droplets by turbulent collision coalescence”, *J. Atmos. Sci.*, vol. 65, pp. 331–356, 2008.
- [30] C. Franklin, “A warm rain microphysics parameterization that includes the effect of turbulence”, *J. Atmos. Sci.*, vol. 65, pp. 1795–1816, 2008.
- [31] E. Bodenschatz, S. Malinowski, R. Shaw, and F. Stratmann, “Can we understand clouds without turbulence?”, *American Association for the Advancement of Science*, vol. 327, pp. 970–971, 2010.

- [32] P. Vaillancourt, M. Yau, P. Bartello, and W. Grabowski, "Microscopic approach to cloud droplet growth by condensation. Part II: Turbulence, clustering, and condensational growth", *J. Atmos. Sci.*, vol. 59, pp. 3421–3435, 2002.
- [33] M.R. Maxey and J.J. Riley, "Equation of motion for a small rigid sphere in a nonuniform flow", *Phys. Fluids*, vol. 26, p. 883, 1983.
- [34] P. Dimotakis, "Turbulent mixing", *Annu. Rev. Fluid Mech.*, vol. 37, pp. 329–356, 2005.
- [35] J. Westerweel, C. Fukushima, J. M. Pedersen, and J. Hunt, "Momentum and scalar transport at the turbulent/non-turbulent interface of a jet", *J. Fluid Mech.*, vol. 631, pp. 199–230, 2009.
- [36] A.M. Blyth, W.A. Cooper and J.B. Jensen, "A study of the source of entrained air in montana cumuli" *J. Atmos. Sci.* 45, 3944–3964, 1988.
- [37] Stevens, Bjorn "Atmospheric moist convection. *Annual Review of Earth and Planetary Sciences*" 33, 605–43, 2005.
- [38] J. Brenguier and W. Grabowski, "Cumulus entrainment and cloud droplet spectra: a numerical model within a two-dimensional dynamical framework", *J. Atmos. Sci.*, vol. 50, pp. 120–136, 1993.
- [39] A. Augustin; J. Yi; T. Clausen; W. Townsley, "A Study of LoRa: Long Range & Low Power Networks for the Internet of Things". *Sensors* 16, 1466, 2016.
- [40] L.F. Richardson; G.T. Walker, "Atmospheric Diffusion Shown on a Distance-Neighbour Graph". *Proc. R. Soc. Lond. Ser. Contain. Pap. Math. Phys. Character*, 110, 709–737, 1926.
- [41] M.E. Paredes Quintanilla; S. Abdunabiev; M. Allegretti; A. Merlone; C. Musacchio; E.G.A. Pasero; D. Tordella; F. Canavero, "Innovative Mini Ultralight Radioprobes to Track Lagrangian Turbulence Fluctuations within Warm Clouds: *Electronic Design. Sensors*" 2021, 21, 1351. [Online] Available: <https://doi.org/10.3390/s21041351>
- [42] J.C. Hubbert; J.W. Wilson; T.M. Weckwerth; S.M. Ellis; M. Dixon; E. Loew, "S-Pol's Polarimetric Data Reveal Detailed Storm Features (and Insect Behavior)". *Bull. Am. Meteorol. Soc.* 2018, 99, 2045–2060.
- [43] S.P. Malinowski; H. Gerber; I. Jen-La Plante; M.K. Kopec; W. Kumala; K. Nurowska; P.Y. Chuang; D. Khelif; K.E. Haman, "Physics of Stratocumulus Top (POST): Turbulent Mixing across Capping Inversion." *Atmos. Chem.*
- [44] W.A. Hoppel; G.M. Frick; J.W. Fitzgerald; B.J. Wattle, "A Cloud Chamber Study of the Effect That Nonprecipitating Water Clouds Have on the Aerosol Size Distribution". *Aerosol Sci. Technol.* 1994, 20, 1–30.
- [45] K. Chang; J. Bench; M. Brege; W. Cantrell; K. Chandrakar; D. Ciochetto; C. Mazzoleni; L.R. Mazzoleni; D. Niedermeier; R.A. Shaw, "A Laboratory Facility to Study Gas–Aerosol–Cloud Interactions in a Turbulent Environment: The P Chamber". *Bull. Am. Meteorol. Soc.* 2016, 97, 2343–2358.
- [46] B. Kumar; P. Götzfried; N. Suresh; J. Schumacher; R.A. Shaw, "Scale Dependence of Cloud Microphysical Response to Turbulent Entrainment and Mixing". *J. Adv. Model. Earth Syst.* 2018, 10, 2777–2785.

- [47] B. Kumar; J. Schumacher; R.A. Shaw, Lagrangian Mixing Dynamics at the Cloudy-Clear Air Interface. *J. Atmos. Sci.* 2014, 71, 2564–2580.
- [48] CORDIS; European Commission. Cloud-MicroPhysics-Turbulence-Telemetry: An Inter-Multidisciplinary Training Network for Enhancing the Understanding and Modeling of Atmospheric Clouds. COMPLETE Project. H2020. [Online] Available : <https://cordis.europa.eu/project/id/675675>.
- [49] S.J. Fletcher, "Observations. In *Data Assimilation for the Geosciences*"; Elsevier: Amsterdam, The Netherlands, 2017; pp. 599–626. ISBN 978-0-12-804444-5.
- [50] F. Toschi; E. Bodenschatz, "Lagrangian Properties of Particles in Turbulence". *Annu. Rev. Fluid Mech.* 2009, 41, 375–404.
- [51] Turbulent Particle Pair Diffusion: A Theory Based on Local and Non-Local Diffusional Processes. [Online] Available: <https://journals.plos.org/plosone/article?id=10.1371/journal.pone.0202940>
- [52] Horizon 2020; Call: H2020-MSCA-ITN-2015-ETN - Proposal Submission Forms”, Research Executive Agency, vol. 675675, 2015.
- [53] M. Paredes; S. Bertoldo; C. Lucianaz; M. Allegretti, “Ultra-light disposable radio probes for atmospheric monitoring”, *EGU General Assembly Conference Abstracts*, vol. 20, p. 1389, 2018.
- [54] CLOUD-MyPhyTuTel, “Ideas concerning ultra-light radiosondes”, 2014.
- [55] M. Paredes, “COMPLETE Workshop: Data and model integration in fluid mechanics”, Imperial College London, December 17 - 19 2019.
- [56] https://www.bosch_sensortec.com/media/boschsensortec/downloads/datasheets/bstbme280-ds002.pdf
- [57] A. Wixted; P. Kinnaird; H. Larijani; A. Tait; A. Ahmadinia; N. Strachan, “Evaluation of LoRa and LoRawan for wireless sensor networks”, 2016 *IEEE SENSORS*, pp. 1–3, 2016.
- [58] T. Basso; G. Perotto; C. Musacchio; A. Merlone; A. Athanassiou; D. Tordella, “Evaluation of Mater Bi PolyLactic Acid as materials for biodegradable innovative mini-radiosondes to track small scale fluctuations within clouds”, *Materials Chemistry and Physics*, vol. 253, p. 123 411, 2020.
- [59] K.B. Cooper; G. Chattopadhyay, "Submillimeter-Wave Radar: Solid-State System Design and Applications". *IEEE Microw. Mag.* 2014, 15, 51–67.
- [60] Bosh BME280 Combine humidity and pressure sensor [Online] Available: <https://www.bosch-sensortec.com/media/boschsensortec/downloads/datasheets/bst-bme280-ds002.pdf>
- [61] M. Golshan; S. Abdunabiev ; M. Tomatis; F. Fraternali; M. Vanni; D. Tordella, " Intermittency acceleration of water droplet population dynamics inside the interfacial layer between cloudy and clear air environments"; *International Journal of Multiphase Flow*, 140, 103669.